



National Library
of Canada

Acquisitions and
Bibliographic Services Branch

395 Wellington Street
Ottawa, Ontario
K1A 0N4

Bibliothèque nationale
du Canada

Direction des acquisitions et
des services bibliographiques

395, rue Wellington
Ottawa (Ontario)
K1A 0N4

Your file *Votre référence*

Our file *Notre référence*

The author has granted an irrevocable non-exclusive licence allowing the National Library of Canada to reproduce, loan, distribute or sell copies of his/her thesis by any means and in any form or format, making this thesis available to interested persons.

L'auteur a accordé une licence irrévocable et non exclusive permettant à la Bibliothèque nationale du Canada de reproduire, prêter, distribuer ou vendre des copies de sa thèse de quelque manière et sous quelque forme que ce soit pour mettre des exemplaires de cette thèse à la disposition des personnes intéressées.

The author retains ownership of the copyright in his/her thesis. Neither the thesis nor substantial extracts from it may be printed or otherwise reproduced without his/her permission.

L'auteur conserve la propriété du droit d'auteur qui protège sa thèse. Ni la thèse ni des extraits substantiels de celle-ci ne doivent être imprimés ou autrement reproduits sans son autorisation.

ISBN 0-612-16480-2

Canada

Name WAYNE ALAN BARKHAUSE

Dissertation Abstracts International is arranged by broad, general subject categories. Please select the one subject which most nearly describes the content of your dissertation. Enter the corresponding four-digit code in the spaces provided.

Astronomy AND Astrophysics
SUBJECT TERM

0606 U-M-I
SUBJECT CODE

Subject Categories

THE HUMANITIES AND SOCIAL SCIENCES

COMMUNICATIONS AND THE ARTS

Architecture 0729
 Art History 0377
 Cinema 0900
 Dance 0378
 Fine Arts 0357
 Information Science 0723
 Journalism 0391
 Library Science 0399
 Mass Communications 0708
 Music 0413
 Speech Communication 0459
 Theater 0465

EDUCATION

General 0515
 Administration 0514
 Adult and Continuing 0516
 Agricultural 0517
 Art 0273
 Bilingual and Multicultural 0282
 Business 0688
 Community College 0275
 Curriculum and Instruction 0727
 Early Childhood 0518
 Elementary 0524
 Finance 0277
 Guidance and Counseling 0519
 Health 0680
 Higher 0745
 History of 0520
 Home Economics 0278
 Industrial 0521
 Language and Literature 0279
 Mathematics 0280
 Music 0522
 Philosophy of 0998
 Physical 0523

Psychology 0525
 Reading 0535
 Religious 0527
 Sciences 0714
 Secondary 0533
 Social Sciences 0534
 Sociology of 0340
 Special 0529
 Teacher Training 0530
 Technology 0710
 Tests and Measurements 0288
 Vocational 0747

LANGUAGE, LITERATURE AND LINGUISTICS

Language

General 0679
 Ancient 0289
 Linguistics 0290
 Modern 0291

Literature

General 0401
 Classical 0294
 Comparative 0293
 Medieval 0297
 Modern 0298
 African 0316
 American 0591
 Asian 0305
 Canadian (English) 0352
 Canadian (French) 0355
 English 0593
 Germanic 0311
 Latin American 0312
 Middle Eastern 0315
 Romance 0313
 Slavic and East European 0314

PHILOSOPHY, RELIGION AND THEOLOGY

Philosophy 0422

Religion

General 0318
 Biblical Studies 0321
 Clergy 0319
 History of 0320
 Philosophy of 0322
 Theology 0469

SOCIAL SCIENCES

American Studies 0323

Anthropology

Archaeology 0324
 Cultural 0326
 Physical 0327

Business Administration

General 0310
 Accounting 0272
 Banking 0770
 Management 0454
 Marketing 0338
 Canadian Studies 0385

Economics

General 0501
 Agricultural 0503
 Commerce-Business 0505
 Finance 0508
 History 0509
 Labor 0510
 Theory 0511

Folklore 0358

Geography 0366

Gerontology 0351

History

General 0578

Ancient 0579
 Medieval 0581
 Modern 0582
 Black 0328
 African 0331
 Asia, Australia and Oceania 0332
 Canadian 0334
 European 0335
 Latin American 0336
 Middle Eastern 0333
 United States 0337
 History of Science 0585
 Law 0398
 Political Science

General 0615

International Law and Relations 0616
 Public Administration 0617
 Recreation 0814
 Social Work 0452

Sociology

General 0626
 Criminology and Penology 0627
 Demography 0938
 Ethnic and Racial Studies 0631
 Individual and Family Studies 0628
 Industrial and Labor Relations 0629
 Public and Social Welfare 0630
 Social Structure and Development 0700
 Theory and Methods 0344
 Transportation 0709
 Urban and Regional Planning 0999
 Women's Studies 0453

THE SCIENCES AND ENGINEERING

BIOLOGICAL SCIENCES

Agriculture

General 0473
 Agronomy 0285
 Animal Culture and Nutrition 0475
 Animal Pathology 0476
 Food Science and Technology 0359
 Forestry and Wildlife 0478
 Plant Culture 0479
 Plant Pathology 0480
 Plant Physiology 0817
 Range Management 0777
 Wood Technology 0746

Biology

General 0306
 Anatomy 0287
 Biostatistics 0308
 Botany 0309
 Cell 0379
 Ecology 0329
 Entomology 0353
 Genetics 0369
 Limnology 0793
 Microbiology 0410
 Molecular 0307
 Neuroscience 0317
 Oceanography 0416
 Physiology 0433
 Radiation 0821
 Veterinary Science 0778
 Zoology 0472

Biophysics

General 0786
 Medical 0760

EARTH SCIENCES

Biogeochemistry 0428
 Geochemistry 0996

Geodesy 0370
 Geology 0372
 Geophysics 0373
 Hydrology 0388
 Mineralogy 0411
 Paleobotany 0345
 Paleocology 0426
 Paleontology 0418
 Paleozoology 0985
 Paleontology 0427
 Physical Geography 0368
 Physical Oceanography 0415

HEALTH AND ENVIRONMENTAL SCIENCES

Environmental Sciences 0768

Health Sciences

General 0566
 Audiology 0300
 Chemotherapy 0992
 Dentistry 0567
 Education 0350
 Hospital Management 0769
 Human Development 0758
 Immunology 0982
 Medicine and Surgery 0564
 Mental Health 0347
 Nursing 0569
 Nutrition 0570
 Obstetrics and Gynecology 0380
 Occupational Health and Therapy 0354
 Ophthalmology 0381
 Pathology 0571
 Pharmacology 0419
 Pharmacy 0572
 Physical Therapy 0382
 Public Health 0573
 Radiology 0574
 Recreation 0575

Speech Pathology 0460
 Toxicology 0383
 Home Economics 0386

PHYSICAL SCIENCES

Pure Sciences

Chemistry

General 0485
 Agricultural 0749
 Analytical 0486
 Biochemistry 0487
 Inorganic 0488
 Nuclear 0738
 Organic 0490
 Pharmaceutical 0491
 Physical 0494
 Polymer 0495
 Radiation 0754
 Mathematics 0405

Physics

General 0605
 Acoustics 0986
 Astronomy and Astrophysics 0406
 Atmospheric Science 0608
 Atomic 0748
 Electronics and Electricity 0607
 Elementary Particles and High Energy 0798
 Fluid and Plasma 0759
 Molecular 0409
 Nuclear 0610
 Optics 0752
 Radiation 0756
 Solid State 0411
 Statistics 0463

Applied Sciences

Applied Mechanics 0346
 Computer Science 0984

Engineering

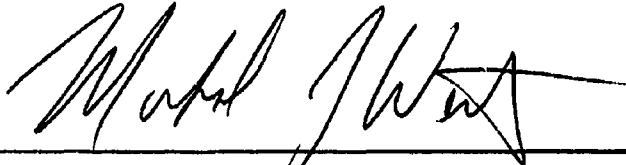
General 0537
 Aerospace 0538
 Agricultural 0539
 Automotive 0540
 Biomedical 0541
 Chemical 0542
 Civil 0543
 Electronics and Electrical 0544
 Heat and Thermodynamics 0348
 Hydraulic 0545
 Industrial 0546
 Marine 0547
 Materials Science 0794
 Mechanical 0548
 Metallurgy 0743
 Mining 0651
 Nuclear 0582
 Packaging 0549
 Petroleum 0765
 Sanitary and Municipal 0684
 System Science 0790

Geotechnology 0428
 Operations Research 0796
 Plastics Technology 0795
 Textile Technology 0994

PSYCHOLOGY

General 0621
 Behavioral 0384
 Clinical 0422
 Developmental 0420
 Experimental 0423
 Industrial 0424
 Personality 0425
 Physiological 0989
 Psychobiology 0349
 Psychometrics 0632
 Social 0481

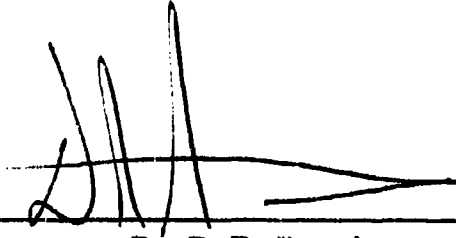
The Examining Committee



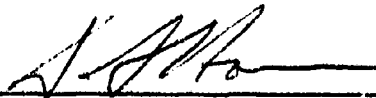
Dr. M. J. West (Thesis Supervisor)
Associate Professor of Astronomy and Physics
Saint Mary's University



Dr. M. N. Butler
Associate Professor of Astronomy and Physics
Saint Mary's University



Dr. D. B. Guenther
Associate Professor of Astronomy and Physics
Saint Mary's University



Dr. D. A. Hanes
Professor of Physics
Queen's University

Abstract

Globular Cluster Populations of Hickson Compact Groups

Wayne A. Barkhouse

September 1996

We present deep V and R band CCD photometry of the globular cluster systems of Hickson compact group galaxy 22a (NGC 1199) and 90c (NGC 7173), taken with the European Southern Observatory's New Technology Telescope (NTT). Globular cluster populations were detected in both galaxies, with HCG 22a having a specific frequency of $S_N \sim 2$ and HCG 90c having a value of $S_N \sim 4$. Both values of specific frequency are consistent with the average value found for field ellipticals. These results give rise to two possible scenarios for globular cluster formation in these galaxies; a) globular clusters formed during the time when their parent galaxy was simply a 'field' galaxy, or b) mergers are not important in the formation of globular clusters in Hickson compact groups (Hickson compact groups are expected to have high merger rates due to their large densities and low velocity dispersions).

Acknowledgment

I would like to thank a large number of people who have helped to make the completion of this thesis possible. For helpful comments and suggestions I would like to thank Greg Bothun, Terry Bridges, Pat Durrell, William Harris, Rachael Webster, and Frank Valdes. I would also like to thank the graduate students at Saint Mary's University for support during the long hours needed to complete this thesis. Special thanks go to Melvin Blake, Mike Casey, Kevin Douglas, Stefan Elieff, Todd Fuller, Gary Gidney, Bev Miskolczi and Steve Short.

Many thanks to the faculty at Saint Mary's for many enlightening discussions about astronomy. Thanks to professors Malcolm Butler, David Clarke, David Guenther, George Mitchell, David Turner, Gary Welch and Michael West. Also thanks to technician and computer expert David Lane for solving many computer related problems.

I would also like to thank the members of my examining committee; Malcolm Butler, David Guenther, David Hanes and Michael West. I would like to extend special thanks to David Hanes whose helpful comments and suggestions have greatly improved the quality of the work presented here.

Very special thanks goes out to Michael West for being my supervisor and providing the necessary data and encouragement to undertake and complete this study (and for putting up with me for 18 months!).

Finally, I would like to thank Janet Benoit for understanding the large amounts of time needed to complete this study.

Contents

1	INTRODUCTION	7
1.1	Globular Clusters	7
1.2	Specific Frequency	8
1.3	Purpose of this study	9
1.4	HCG 22 and HCG 90	11
2	DATA REDUCTIONS	15
2.1	Observations	15
2.2	Preprocessing	18
2.3	Standard Star Reductions	19
2.4	Galaxy and Control Field Processing	24
2.5	Galaxy Light Removal	30
2.6	FOCAS	33
2.7	Instrumental Magnitudes	37
2.8	Standard Magnitudes	42
3	Data Analysis	43
3.1	Completeness Tests	43
3.2	Final Object List	47
3.3	Photometric Errors	49
3.3.1	Systematic Errors	51
3.3.2	Random Errors	55

4	Results	57
4.1	Globular Cluster Luminosity Function	57
4.1.1	HCG 22a	58
4.1.2	HCG 90c	60
4.2	Radial Distribution: HCG 22a	62
4.3	Radial Distribution: HCG 90c	67
4.4	Specific Frequency: HCG 22a	68
4.5	Specific Frequency: HCG 90c	71
5	Discussion	73
6	Summary and Conclusion	76
7	References	77
	Appendix A	81
	Appendix B	87

List of Figures

1.1	Mean specific globular cluster frequency as a function of local environment.	9
1.2	Image of HCG 22 taken from the Digital Sky Survey.	12
1.3	Image of HCG 90 taken from the Digital Sky Survey.	14
2.1	Plot of residuals (magnitude units) versus V magnitude (from fitting function) for October 9 standard star photometry.	22
2.2	Plot of residuals (magnitude units) versus V-R from the V transformation equation using standard star photometry from October 9. . .	22
2.3	Plot of residuals (magnitude units) versus R magnitude (from fitting function) for October 9 standard star photometry.	23
2.4	Plot of residuals (magnitude units) versus V-R from the R transformation equation using standard star photometry from October 9. . .	23
2.5	HCG 22a.	27
2.6	HCG90c (slightly right of centre)	28
2.7	Control field.	29
2.8	STSDAS/Bmodel subtracted image of HCG 22a.	31
2.9	Median filtered subtracted image of HCG 22a.	32
2.10	Median filtered subtracted image of HCG 90c.	34
2.11	Plot of FOCAS scale parameter versus V magnitude for HCG 22a. . .	37
2.12	Plot of FOCAS scale parameter versus V magnitude for HCG 90c. . .	38
2.13	Plot of FOCAS scale parameter versus V magnitude for the control field.	38

2.14	Plot of S/N versus aperture radius.	39
2.15	Plot of the adopted curve-of-growth profile.	41
3.1	Completeness function for HCG 22a.	45
3.2	Completeness function for HCG 90c.	47
3.3	Completeness function for the control field.	48
3.4	Colour-magnitude plot of the globular cluster candidates surrounding HCG 22a.	50
3.5	Colour-magnitude plot of star-like objects surrounding HCG 90c. . .	50
3.6	Colour-magnitude plot of star-like objects in the control field.	51
3.7	Positions of globular cluster candidates surrounding HCG 22a.	52
3.8	Positions of globular cluster candidates surrounding HCG 90c.	53
3.9	A plot of the standard deviation versus V magnitude for the globular cluster candidates in HCG 22a.	54
3.10	A plot of the standard deviation versus V magnitude for the globular cluster candidates in HCG 90c.	54
3.11	Plot of the magnitude difference between added artificial stars and recovered star in HCG 22a.	55
3.12	Plot of the magnitude difference between added artificial stars and recovered stars in HCG 90c.	56
4.1	Globular cluster luminosity function for HCG 22a.	61
4.2	Globular cluster luminosity function for HCG 90c.	63
4.3	Radial distribution of globular clusters around HCG 22a.	65
4.4	Comparison of the radial profile of GCs versus galaxy surface brightness for HCG 22a.	66
4.5	Radial distribution of globular clusters around HCG 90c.	68

List of Tables

1.1	General properties of HCG 22a (NGC 1199) from Hickson (1994). . .	10
1.2	General properties of HCG 90c (NGC 7173) from Hickson (1994). . .	10
2.1	CCD/Telescope Parameters	16
2.2	Observations of HCG 22a.	16
2.3	Observations of HCG 90c.	17
2.4	Observation log of control field.	17
2.5	Observations of Standard Stars.	18
2.6	Transformation Coefficients	21
2.7	Standard Star Photometry For October.9	24
2.8	Standard star instrumental magnitudes.	25
2.9	Seeing log for combined images.	28
2.10	Classification Rules	35
2.11	Aperture Correction	42
3.1	Completeness Data For HCG 22a.	45
3.2	Completeness Data For HCG 90c.	46
3.3	Completeness Data For Control Field.	48
4.1	Globular Cluster Luminosity Function Data: HCG 22a.	59
4.2	Globular Cluster Luminosity Function Data: HCG 90c.	62
4.3	GCLF turnover apparent magnitudes.	62
4.4	Globular Cluster Radial Distribution Data: HCG 22a.	64
4.5	Globular Cluster Radial Distribution Data: HCG 90c.	67

4.6	Summary of specific frequency values.	72
A.1	Photometry of globular cluster candidates in HCG 22a.	82
A.2	HCG 22a photometry—Continued	83
A.3	HCG 22a photometry—Continued	84
A.4	HCG 22a photometry—Continued	85
A.5	HCG 22a photometry—Continued	86
B.1	Photometry of globular cluster candidates in HCG 90c.	88
B.2	HCG 90c photometry—Continued	89
B.3	HCG 90c photometry—Continued	90
B.4	HCG 90c photometry—Continued	91
B.5	HCG 90c photometry—Continued	92
B.6	HCG 90c photometry—Continued	93
B.7	HCG 90c photometry—Continued	94

Chapter 1

INTRODUCTION

1.1 Globular Clusters

Globular clusters (GCs) are one of the oldest stellar populations that exist today. They are generally comprised of up to $\sim 10^5 - 10^6$ stars and are found mainly in the halo of most galaxies. The Milky Way contains over 100 globular clusters whose ages range from 10 to 16 Gyrs, although the determination of the absolute ages of globular clusters has been controversial (see; e.g., Chaboyer, Demarque & Sarajedini 1996; Stetson, Vandenberg & Bolte 1996; Jimenez et al. 1996). Since globular clusters are among the oldest objects in the Universe, they provide a valuable probe of the conditions that existed at time of their formation and hence may also provide important insights to galaxy formation (e.g., Eggen, Lynden-Bell & Sandage 1963; Searle & Zinn 1978). The ages of globular clusters also provide a well-known constraint on the age of the Universe since they must be younger than the Universe in which they exist (e.g., Chaboyer et al. 1996).

With the advent of Charge Coupled Devices (CCDs), tremendous progress has been made over the past decade in the detection of globular clusters around galaxies beyond the Local Group (see Harris 1991, 1993 for reviews). To date, globular cluster populations have been studied in over 70 galaxies, some as far as away as ~ 100 Mpc (e.g., Thompson & Valdes 1987; Harris 1987). Studies have shown that the number of globular clusters associated with any particular galaxy varies widely from ~ 0 for M32 (NGC 221) to over 16,000 for the cD galaxy M87 (e.g., Harris 1991).

1.2 Specific Frequency

A useful method of quantifying the total number of globular clusters per galaxy is the *specific frequency*, S_N , which is defined as the total number of globular clusters per unit galaxy luminosity (normalized to $M_v = -15$) and is given by (Harris & van den Bergh 1981)

$$S_N = N_{tot} \times 10^{0.4(M_v+15)},$$

where

N_{tot} = the total number of globular clusters,

M_v = the total absolute V magnitude of the parent galaxy.

One of the most important results to come out of previous work has been the discovery that globular cluster populations vary systematically with galaxy type and environment (see Figure 1.1; also Harris 1991). Characteristic values of S_N range from $S_N \leq 1$ for field spiral galaxies, to $S_N \simeq 2-3$ for field ellipticals, to $S_N \simeq 5-7$ for ellipticals in rich galaxy clusters and up to $S_N \simeq 10-20$ for cD galaxies at the centres of rich clusters. Yet, which factor has the greatest influence on globular cluster formation—galaxy type or environment—is unclear. As an example of an exception to the general trends mentioned above, Harris, Pritchett & McClure (1995) have shown that NGC 7768 (a cD galaxy in the rich Abell cluster A2666) has a specific frequency of only ~ 4 while M87 (a galaxy similar to NGC 7768 in terms of local environment and absolute luminosity) has a specific frequency of ~ 14 .

Harris et al. (1995) have recently reviewed the possible correlation between specific frequency and a wide range of possible environmental factors. These factors include: a) cooling flow rates; b) X-ray luminosity of intracluster gas; c) total mass of intracluster gas; d) X-ray temperature of the intracluster gas and e) Bautz–Morgan type of the host galaxy cluster. No significant correlation was found for any of the above mentioned factors with specific frequency (however; see West et al. 1995).

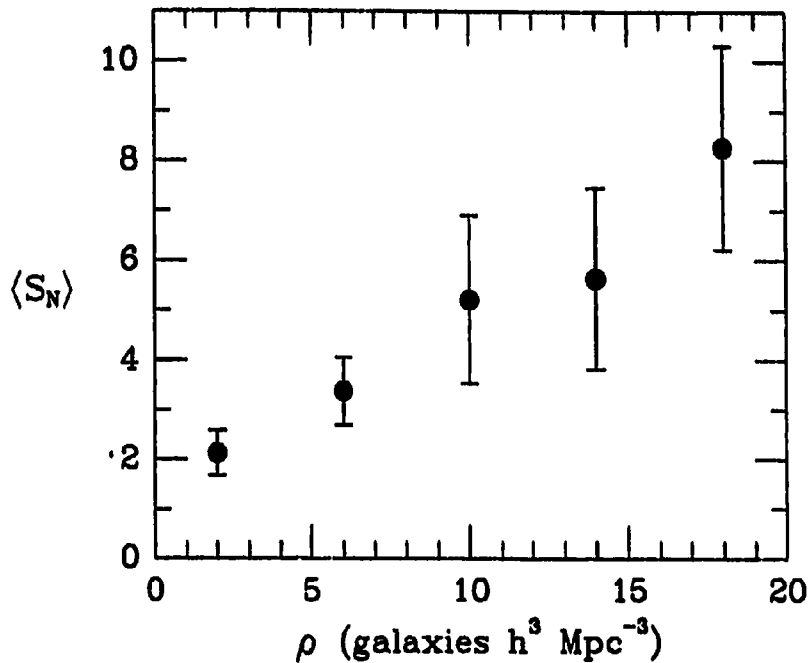


Figure 1.1: Mean specific globular cluster frequency as a function of local environment (from West 1993). S_N values are primarily from the compilation by Harris (1991). Local galaxy density ρ is based on the distribution of galaxies in Tully's (1988) *Nearby Galaxies Catalog*.

1.3 Purpose of this study

A better understanding of the environmental dependence of globular cluster populations is crucial for constraining competing theories of GC formation (e.g., Fall & Rees 1985; Harris & Pudritz 1994) such as cooling flows (Fabian, Nulsen & Canizares 1984), galaxy mergers (Ashman & Zepf 1992), 'biased' globular cluster formation (West 1993) and intracluster globular clusters (West et al. 1995). Thus it is essential that the specific frequency be measured for galaxies in as wide a range of environments as possible. Yet to date only a limited range of galaxy environments have been explored.

The purpose of this study is to measure the globular cluster populations of two galaxies in Hickson compact groups; HCG 22a (NGC 1199) and HCG 90c (NGC 7173) (see Tables 1.1 and 1.2 for summary of general properties of these two galaxies). Hickson compact groups are extremely interesting environments because, although

Table 1.1: General properties of HCG 22a (NGC 1199) from Hickson (1994).

Quantity	Value
α (1950)	$03^h 01^m 18.2^s$
δ (1950)	$-15^\circ 48' 30''$
l	$199^\circ.22$
b	$-57^\circ.31$
Hubble Type	E2
V_o (heliocentric)	2705 km/s
B_T	12.24
B-R	1.62

Table 1.2: General properties of HCG 90c (NGC 7173) from Hickson (1994).

Quantity	Value
α (1950)	$21^h 59^m 08.8^s$
δ (1950)	$-32^\circ 12' 58''$
l	$14^\circ.98$
b	$-53^\circ.08$
Hubble Type	E0
V_o (heliocentric)	2696km/s
B_T	12.73
B-R	2.23

they are small (typically 3–7 member galaxies per group), they are extremely dense systems, comparable in density to the cores of rich Abell clusters (e.g., Hickson 1982; Hickson et al. 1992). This makes them invaluable tools for probing the influence of environment on globular cluster formation. No other study to date has examined the globular cluster system of any Hickson compact group member.

Hickson (1982) identified one hundred compact groups from the Palomar Observatory Sky Survey red prints using three basic criteria: a) population – groups must contain at least four members within three magnitudes of the brightest galaxy; b) isolation – the radius of the smallest circle containing the centres of the galaxies must be at least one third of the radius of a circle containing the centre of a non-member galaxy satisfying the same magnitude criterion; and c) compactness – the surface brightness averaged over the area of the smallest circle containing the centres of the

member galaxies must be $\mu_R < 26 \text{ mag/arcsec}^2$.

Since 1982, many studies have examined the properties of compact groups and some controversy exists as to which groups are true compact groups and which are the centres of larger clusters or chance projections of unrelated galaxies (e.g., Williams & Rood 1987; Rood & Williams 1989; Ostriker, Lubin & Hernquist 1995). Some Hickson compact groups have also been detected in X-rays by ROSAT, including HCG 22 and HCG 90 (e.g., Ebeling, Voges & Böhringer 1994; Ponman & Bertram 1993; Pildis, Bregman & Evrard 1995; Ponman et al. 1996). Radial velocity measurements suggest that HCG 22a and HCG 90c are members of their associated group (Hickson et al. 1992) and thus the study of their globular cluster systems should provide clues as to whether these galaxies evolved in a high density environment or were simply field galaxies that have only recently ($\sim 1 - 2 \text{ Gyrs}$) become members of a compact group.

1.4 HCG 22 and HCG 90

Hickson compact group 22 was originally comprised of five members (three ellipticals and two spirals; Hickson (1982)) but later redshift measurements showed that two of the elliptical galaxies (HCG 22d and HCG 22e) are most likely background galaxies with heliocentric radial velocities $\sim 7000 \text{ km/s}$ greater than the remaining group members (Hickson et al. 1992). Figure 1.2 shows an optical image of HCG 22 taken from the Digital Sky Survey.

The median redshift of the member galaxies is $z=0.0090$ and the median radial velocity dispersion (*rms* of the galaxy velocities with respect to the velocity centroid) is 43.7 km/s (Hickson 1994). From Table 1.1, the heliocentric radial velocity for HCG 22a is 2705 km/s which indicates that this galaxy is most likely located nearest to the centre of mass of the group since its redshift is closest to the median value of the group. Hickson et al. (1992) has estimated the mass-to-light ratio of HCG 22 using four different mass estimators (Viral theorem, 'projected', 'average' and 'median') and by dividing the median mass estimate by the group blue luminosity

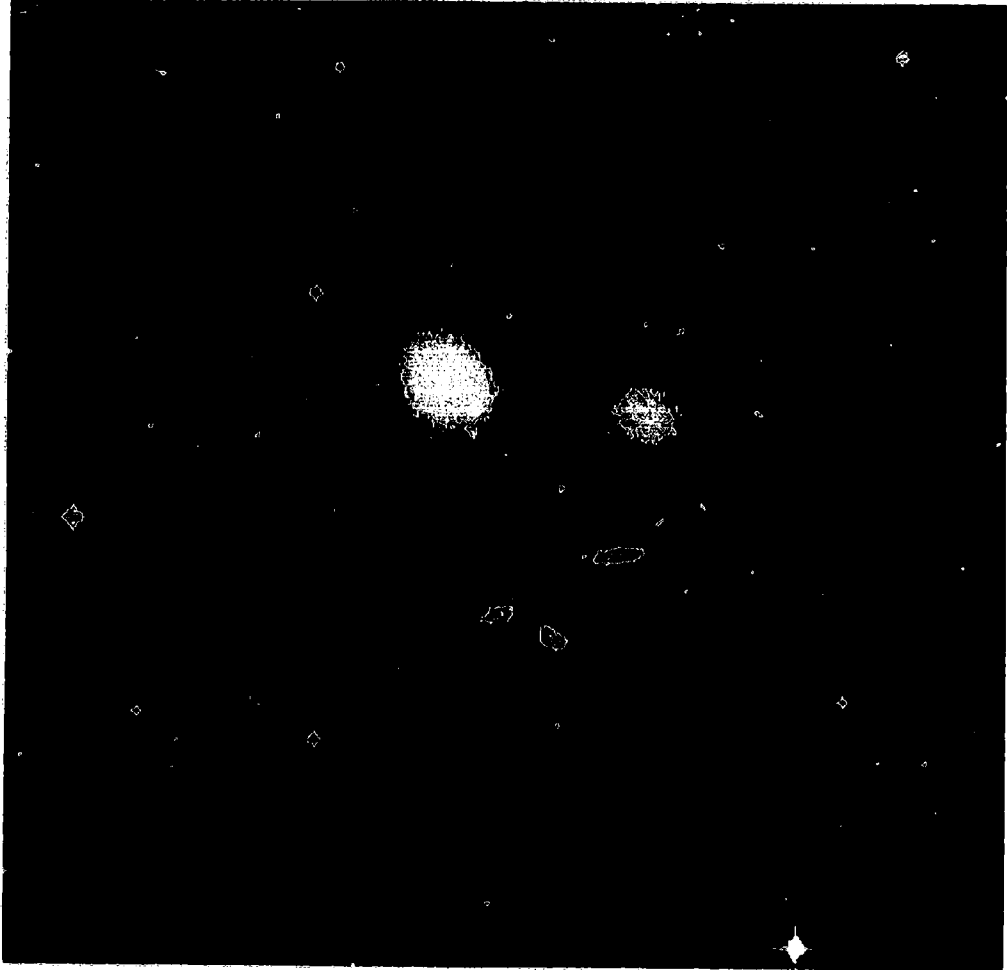


Figure 1.2: Image of HCG 22 taken from the Digital Sky Survey.

(Hickson 1994). The mass-to-light ratio was determined to be 1.3 (solar units) and the projected median galaxy-to-galaxy separation is 26.7 kpc (assuming $H_0 = 100$ km/s/Mpc; Hickson 1994). The estimated group crossing time is given by Hickson et al. (1992) as $Ht_c = 0.1905$, which is a rough ratio of the group crossing time with the age of the Universe. This value is large compared to the median value of all Hickson compact groups ($Ht_c = 0.016$; Hickson et al. 1992) and may indicate that galaxy mergers or interactions are less important for HCG 22 than for other compact groups with smaller crossing times.

Hickson compact group 90 consists of four galaxies (two ellipticals, one spiral and one irregular) with a median group redshift of $z=0.0088$ and a median group velocity dispersion (as defined above for HCG 22) of 100 km/s (Hickson et al. 1992). The mass-to-light ratio (as defined above for HCG 22) is determined to be 12.3 (solar units) with a median projected galaxy separation of 29.5 kpc (for $H_0 = 100$ km/s/Mpc; Hickson 1994). From Table 1.2, the heliocentric radial velocity for HCG 90c is 2696 km/s which indicates that this galaxy is most likely located nearest to the centre of mass of the group since its redshift is closest to the median value of the group.

The group crossing time is given as $Ht_c = 0.0221$ which is only $\sim 12\%$ of the estimated value for HCG 22 (Hickson et al. 1992). Intuitively one may conclude that mergers and galaxy interactions have been more important for HCG 90 than for HCG 22 and it is interesting that HCG 90 contains a galaxy (HCG 90d) that appears to be interacting with other group members (see Figure 1.3, bottom half of figure). HCG 22 and HCG 90 have been detected in X-rays by ROSAT (Ponman et al. 1996) and have measured X-ray luminosities of $\log L_X < 41.14$ ergs/s and $\log L_X = 41.48 \pm 0.09$ ergs/s, respectively. Thus it is important to compare the globular cluster populations of HCG 22a and HCG 90c since these galaxies may have formed their GCs in widely different environments.



Figure 1.3: Image of HCG 90 taken from the Digital Sky Survey.

Chapter 2

DATA REDUCTIONS

2.1 Observations

The data for this thesis were obtained using the 3.5 metre New Technology Telescope (NTT), operated by the European Southern Observatory (ESO) in La Silla, Chile. The observations were taken over a two night period (9-10 October 1993) using remote observing from Garching, Germany, by Dr. Michael J. West. All images were taken with the ESO Multi-Mode Instrument (EMMI) with a Loral 2048 CCD (ESO#34) mounted on the red arm.

The Loral 2048 CCD chip consisted of 2048 x 2048 pixel area with a pixel size of $15 \times 15 \mu m$. Technical limitations at the time forced a reduction of the effective area of the chip to 1700 x 1700 pixels, including the loss of the overscan region in all frames. The scale of the telescope/detector combination (F/11 Nasmyth focus) was $\sim 0.289''/\text{pixel}$ which gives a projected area on the sky of $8.2' \times 8.2'$ for each raw frame. A summary of the characteristics of the detector/telescope combination is given in Table 2.1.

The raw data for this study consists of a series of twelve exposures of HCG 90c and ten exposures of HCG 22a in the Cousins V and R passband. In addition to the target galaxies, a series of ten exposures was obtained of a 'control' or background field. Since globular clusters are detected as a statistical excess of star-like objects, the control field is used as a means of setting the 'background' level of star-like objects in a random field. The control field was located within $\sim 3^\circ$ in galactic latitude

Table 2.1: CCD/Telescope Parameters

CCD Chip:	Loral 2048 (ESO # 34)
Format:	2048 x 2048
Pixel Size:	15 μ m x 15 μ m
Pixel scale at Nysmuth Focus:	0.289" x 0.289"
Frame Size:	9.9' x 9.9'
Gain:	1.47 \pm 0.03e ⁻ /ADU
Readout Noise:	6.6 \pm 0.5e ⁻ RMS
Dark Current:	2 \pm 1e ⁻ /pixel/hour @ 161 K
Linearity:	Upper Limit 187000 \pm 5000e ⁻ /pixel
Cosmetic Defects:	2 double columns extending length of frame numerous charge traps

Table 2.2: Observations of HCG 22a.

Date (UT)	Start (UT)	Exposure (Sec.)	Filter	Airmass (Mid.)	Seeing (")
Oct.10	05:26:19	900	V	1.06	0.73
Oct.10	05:45:59	900	V	1.04	0.80
Oct.10	06:46:42	900	V	1.03	0.82
Oct.10	07:06:32	900	V	1.04	0.81
Oct.10	08:08:14	900	V	1.13	0.73
Oct.10	06:06:33	900	R	1.03	0.72
Oct.10	06:26:34	900	R	1.03	0.88
Oct.10	07:27:01	900	R	1.06	0.81
Oct.10	07:46:51	900	R	1.09	0.74
Oct.10	08:28:07	900	R	1.18	0.80

of the galaxy fields in order to provide a reasonable estimate of the background level. A summary of the galaxy and control field exposures are given in Tables 2.2-2.4. All derived magnitudes were transformed to the standard UBVRI system by measuring several standard stars from Landolt (1992). A summary of the standard star observations is given in Table 2.5.

Table 2.3: Observations of HCG 90c.

Date (UT)	Start (UT)	Exposure (Sec.)	Filter	Airmass (Mid.)	Seeing (")
Oct.9	00:30:26	900	V	1.02	0.96
Oct.9	00:50:15	900	V	1.01	0.87
Oct.9	01:51:55	900	V	1.01	1.07
Oct.9	02:11:50	900	V	1.02	1.04
Oct.9	03:11:40	900	V	1.08	1.16
Oct.9	03:31:29	900	V	1.12	1.13
Oct.9	01:11:36	900	R	1.00	0.78
Oct.9	01:31:27	900	R	1.00	0.84
Oct.9	02:31:44	900	R	1.03	1.13
Oct.9	02:51:33	900	R	1.06	1.07
Oct.9	03:53:14	900	R	1.17	1.01
Oct.9	04:13:03	900	R	1.23	1.07

Table 2.4: Observation log of control field.

Date (UT)	Start (UT)	Exposure (Sec.)	Filter	Airmass (Mid.)	Seeing (")
Oct.10	01:35:00	900	V	1.00	0.78
Oct.10	01:54:50	900	V	1.01	0.77
Oct.10	02:54:51	900	V	1.07	0.82
Oct.10	03:14:47	900	V	1.10	0.85
Oct.10	04:15:59	900	V	1.25	0.74
Oct.10	02:14:56	900	R	1.02	0.88
Oct.10	02:34:47	900	R	1.04	0.90
Oct.10	03:35:58	900	R	1.14	0.81
Oct.10	03:55:48	900	R	1.19	0.80
Oct.10	04:36:04	900	R	1.33	0.93

Table 2.5: Observations of Standard Stars.

Field	Date (UT)	Start (UT)	Exposure (Sec.)	Filter	Airmass (Mid.)	Seeing (")
PG2213-006	Oct.9	00:18:10	5.00	V	1.24	1.16
Rubin 149	Oct.9	08:48:33	5.00	V	1.34	1.16
Rubin 152	Oct.9	09:08:32	5.00	V	1.27	1.74
PG2213-006	Oct.9	00:12:59	5.00	R	1.25	0.87
Rubin 149	Oct.9	08:53:27	5.00	R	1.32	1.30
Rubin 152	Oct.9	09:13:27	5.00	R	1.26	1.45
PG2213-006	Oct.10	01:09:43	2.00	V	1.15	0.78
PG2331+055	Oct.10	01:20:09	2.00	V	1.36	0.78
Rubin 149	Oct.10	08:48:10	3.00	V	1.32	0.78
PG2213-006	Oct.10	01:15:01	2.00	R	1.15	0.78
PG2331+055	Oct.10	01:25:17	2.00	R	1.34	0.72
Rubin 149	Oct.10	08:53:08	3.00	R	1.31	0.78

2.2 Preprocessing

Before the raw images can be analyzed, they must undergo a series of preprocessing steps. These steps are designed to correct some of the effects that the use of CCD's introduce to the data frames. These steps include the removal of the electronic 'pedestal' level (electronic bias) and the correction for pixel-to-pixel sensitivity variation (flatfield correction). All image processing was performed within the IRAF¹ (Image Reduction and Analysis Facility) environment.

In order to correct for the DC offset or bias, a series of 19 zero second exposure frames were averaged together and the resultant frame subtracted (pixel by pixel) from each image frame using the IRAF routine `Imarith`.

Prior to the subtraction of any bias frame, a separate bias level (calculated from the overscan region) for each individual frame is usually subtracted from the raw image. This overscan bias correction is used to account for any time variation in the bias level. Due to electronic problems during the observing run, no overscan region

¹IRAF is distributed by National Optical Astronomy Observatories, which is operated by the Association of Universities for Research in Astronomy, Inc., under contract to the National Science Foundation.

was recorded for any of the frames. Fortunately, the time variation of the bias level is usually on the order of only 1-2% .

The second step in preprocessing the raw frames is to correct for the fact that the sensitivity of a CCD varies from pixel-to-pixel. This effect is corrected for by dividing each image frame by a 'master' flatfield frame (one per passband since the spatial nonuniformity of the sensitivity is colour dependent). Master flatfield frames were constructed by taking the average over three nights of a series of 15 individual flatfield frames' (per passband; bias corrected) which were created 'by exposing the CCD to a uniformly illuminated source. For this study, the flatfield frames were constructed by taking short exposures of an illuminated portion of the inside of the telescope dome. Flatfield corrections to the data frames produced images which were flat to $\sim 1\%$.

Since the dark current was negligible ($2 \pm 1e^-/\text{pixel}/\text{hour}$) no correction for dark current was attempted. Also, no detectable fringe pattern was evident and hence no fringe correction was performed.

2.3 Standard Star Reductions

The transformation of instrumental to standard magnitudes was accomplished by measuring several standard stars from Landolt (1992) on the nights of October 9 and 10. A total of 19 standard stars were measured on Oct. 9 and 12 stars on Oct. 10, 1993. The IRAF version of DAOPHOT (Stetson, Davis & Crabtree, 1990) was used to perform the photometry and the task PHOTCAL was used to define and solve the transformation equations. The standard star frames were preprocessed in the same way as the galaxy frames and aperture magnitudes were measured using an aperture radius of 15 pixels ($\sim 5 \times$ full-width-half-maximum (FWHM)). All magnitudes were scaled to an exposure time of one second.

The transformation equations were assumed to be of the form:

$$v = V + v_1 + v_2 X_v + v_3(V - R) + v_4(V - R)X_v, \quad (2.1)$$

and

$$r = (V - (V - R)) + r_1 + r_2 X_v + r_3(V - R) + r_4(V - R)X_r, \quad (2.2)$$

where

v = instrumental V magnitude,

V = standard V magnitude,

r = instrumental R magnitude,

R = standard R magnitude,

v_1, v_2, v_3, v_4 = transformation coefficients,

r_1, r_2, r_3, r_4 = transformation coefficients,

X_v = airmass,

X_r = airmass.

The above transformation equations were solved separately for the individual nights and applied to the same night's observations. The transformation coefficients derived for October 10 were found to be unreliable since they gave nonsensical results such as decreasing magnitude with increasing airmass. The most likely cause of this problem is the different influence that the shutter correction (~ 1 second) had on the two and three second exposure fields. The Geneva Observatory located at La Silla reports that the night of Oct. 9, 1993 was photometric and lists extinction coefficients². In order to determine whether Oct. 10 was photometric or not, a comparison was made between images taken on Oct. 9 and 10 of the control field. Using the transformation coefficients from Oct. 9 (for which longer standard star exposures were taken), the magnitudes derived for both nights agree to within ~ 0.015 magnitudes for 16 stars on the control field. These results suggest that both nights were photometric and thus the transformation equation derived for Oct. 9 was used for the data from Oct. 10. From Table 2.5 it is evident that standard star measurements were made over a very narrow range in airmass and thus the Geneva Observatory

²La Silla extinction coefficients can be found at http://www.la.silla.eso.org/la.silla/atm_ext/extinction.html.

Table 2.6: Transformation Coefficients

Date	Coefficient	Value
Oct. 9		
	v_1	0.205 ± 0.002
	v_2	0.189
	v_3	-0.053 ± 0.005
	v_4	0
	r_1	0.050 ± 0.002
	r_2	0.067
	r_3	-0.036 ± 0.007
	r_4	0

extinction coefficients for October 9 1993 were adopted ($v_2 = 0.189$ and $r_2 = 0.067$). The routine in PHOTCAL that solves the transformation equations is the `Fitparams` routine. `Fitparams` allows the user to interactively perform a linear least-squares fit to the standard star data by rejecting spurious data points and including higher order terms in the transformation equations if needed.

A plot of the fitting residuals (magnitude units) versus V magnitude (calculated from the fitting function), for the standard star data from October 9, is presented in Figure 2.1. Three data points have been excluded from the fit (PG2213-006C, RU 149 and RU 152B) due to anomalously high fitting residuals. Figure 2.2 presents a plot of the fitting residuals versus V-R. Since the data points simply scatter about zero, a non-linear colour term is not required.

For the R equation, the above procedure was repeated and data points corresponding to the standard stars RU 149A, RU 149C, RU 152B and RU 152D were rejected as being spurious. Figures 2.3 and 2.4 show plots of the fitting residuals versus R magnitude and V-R for the R transformation equation.

Table 2.6 presents the transformation coefficients derived from standard star observations from October 9 1993.

Table 2.7 list the values of V and V-R for the standard stars, from Landolt (1992), as well as the values derived from the transformation equations. The root-mean-

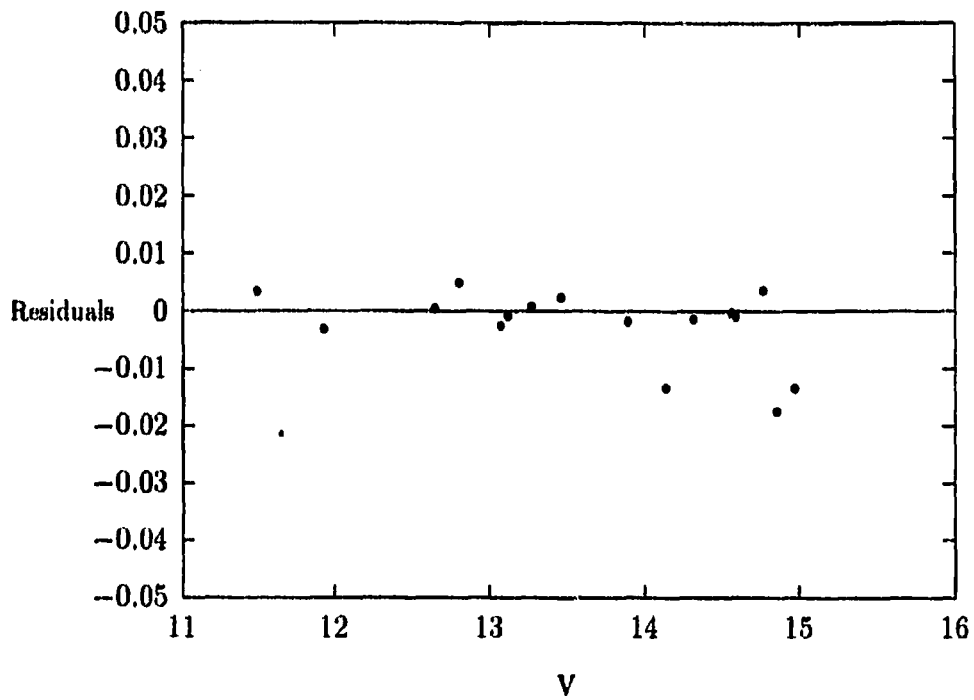


Figure 2.1: Plot of residuals (magnitude units) versus V magnitude (from fitting function) for October 9 standard star photometry.

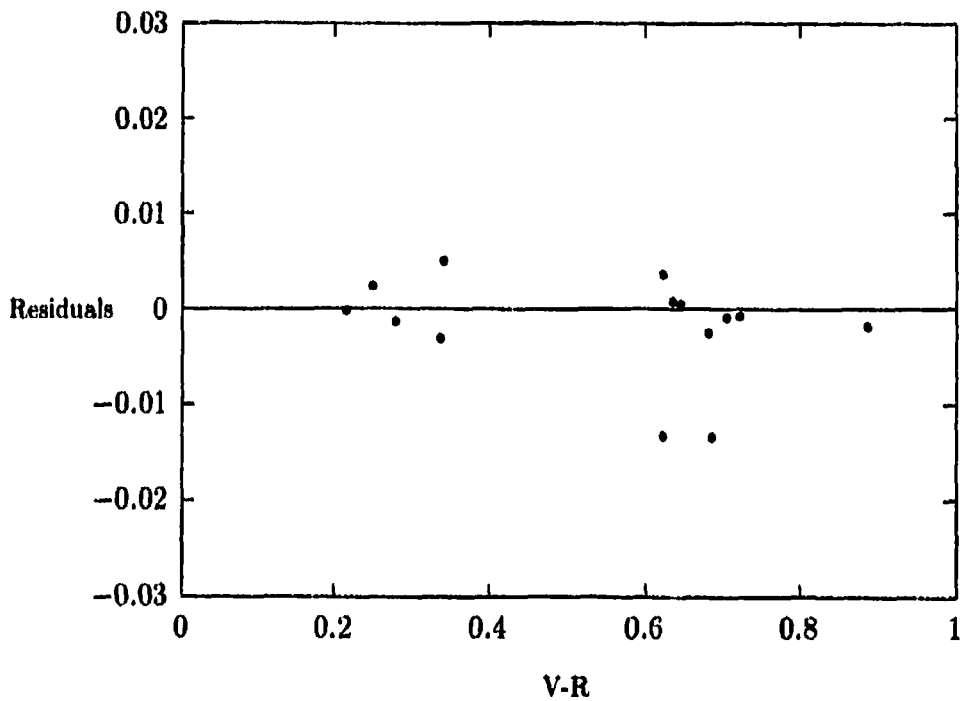


Figure 2.2: Plot of residuals (magnitude units) versus V-R from the V transformation equation using standard star photometry from October 9.

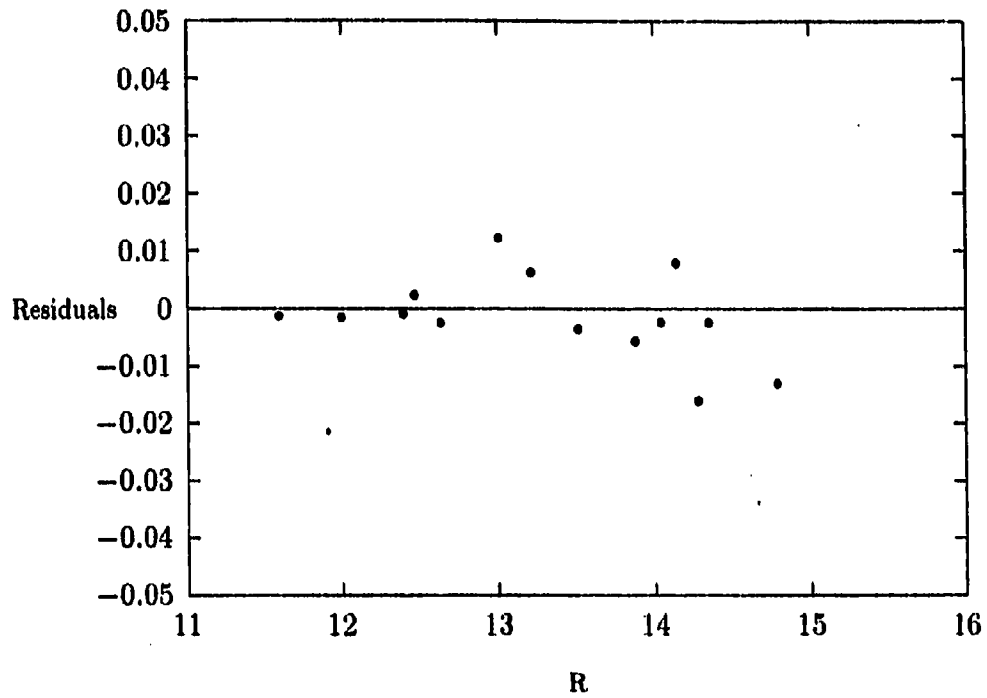


Figure 2.3: Plot of residuals (magnitude units) versus R magnitude (from fitting function) for October 9 standard star photometry.

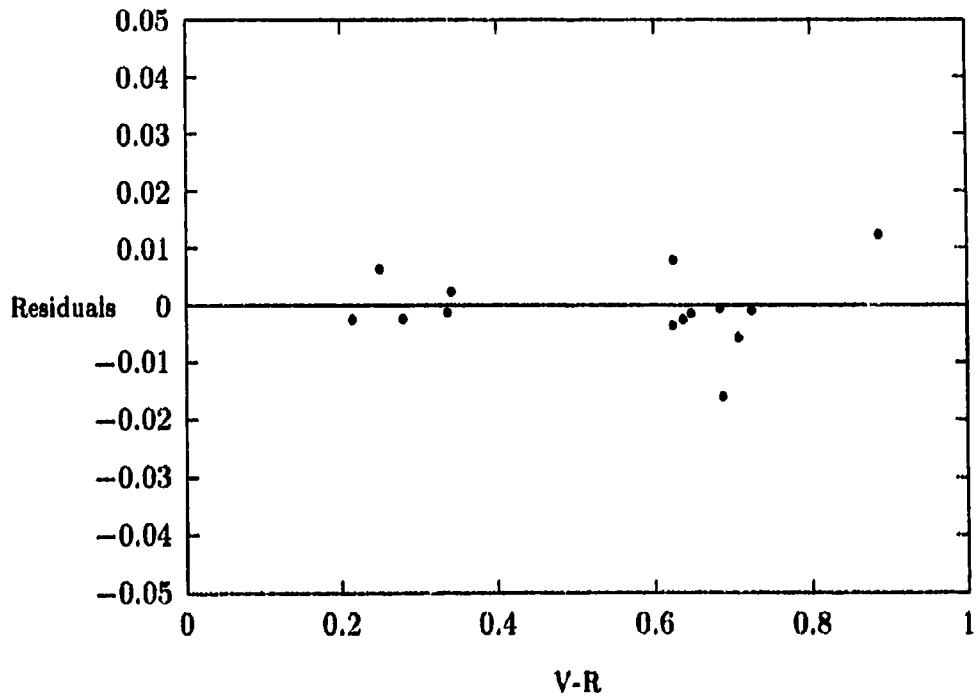


Figure 2.4: Plot of residuals (magnitude units) versus V-R from the R transformation equation using standard star photometry from October 9.

Table 2.7: Standard Star Photometry For October.9

Standard Star ID	Landolt (1992)				Derived Values			
	V	σ_V	V-R	σ_{V-R}	V	σ_V	V-R	σ_{V-R}
PG2213-006	14.124	0.002	-0.092	0.004	14.124	0.004	-0.090	0.006
PG2213-006A	14.178	0.005	0.406	0.003	14.177	0.004	0.411	0.005
PG2213-006B	12.706	0.001	0.427	0.001	12.705	0.002	0.427	0.002
PG2213-006C	15.109	0.004	0.426	0.002	15.082	0.007	0.413	0.009
RU 149	13.866	0.002	-0.040	0.002	13.865	0.004	-0.039	0.006
RU 149A	14.495	0.007	0.196	0.010	14.546	0.008	0.185	0.010
RU 149B	12.642	0.002	0.374	0.002	12.639	0.002	0.372	0.002
RU 149C	14.425	0.005	0.093	0.006	14.408	0.007	0.107	0.009
RU 149D	11.480	0.002	0.021	0.001	11.477	0.001	0.019	0.001
RU 149E	13.718	0.006	0.321	0.004	13.704	0.004	0.311	0.005
RU 149F	13.471	0.003	0.594	0.002	13.468	0.003	0.580	0.004
RU 149G	12.829	0.003	0.322	0.002	12.830	0.002	0.325	0.003
RU 152	13.014	0.002	-0.057	0.002	13.016	0.002	-0.061	0.003
RU 152A	14.341	0.006	0.325	0.005	14.344	0.006	0.321	0.008
RU 152B	15.019	0.005	0.290	0.005	14.983	0.011	0.282	0.014
RU 152C	12.222	0.002	0.342	0.002	12.223	0.001	0.344	0.001
RU 152D	11.076	0.001	0.473	0.001	11.071	0.001	0.320	0.001
RU 152E	12.362	0.001	0.030	0.001	12.367	0.002	0.033	0.002
RU 152F	14.564	0.005	0.382	0.007	14.551	0.007	0.385	0.009

square scatter of the derived V magnitudes, from the values of Landolt (1992), was on the order of $\sigma_V^{ms} \simeq 0.02$ for October 9. Table 2.8 lists the measured instrumental magnitudes for the standard stars from Oct. 9, 1993.

2.4 Galaxy and Control Field Processing

After preprocessing the galaxy images, each series of galaxy frames (per passband) were combined to form a single frame of a higher signal-to-noise ratio (S/N) than the individual frames. In order to combine the images, the frames had to be aligned to a common coordinate system. The IRAF routines `Xregister` and `Imshift` were used to re-register the individual galaxy and control field images to ≤ 0.1 pixels.

Once registered, the V and R images of the galaxies and the control field were median combined using the routine `Imcombine`. The removal of cosmic ray hits (which

Table 2.8: Standard star instrumental magnitudes.

Star	Magnitude	Passband
PG2213-006	14.567	V
PG2213-006	14.351	R
PG2213-006A	14.594	V
PG2213-006A	13.886	R
PG2213-006B	13.121	V
PG2213-006B	12.397	R
PG2213-006C	15.499	V
PG2213-006C	14.789	R
RU 149	14.324	V
RU 149	14.044	R
RU 149A	14.993	V
RU 149A	14.493	R
RU 149B	13.077	V
RU 149B	12.393	R
RU 149C	14.860	V
RU 149C	14.437	R
RU 149D	11.933	V
RU 149D	11.596	R
RU 149E	14.145	V
RU 149E	13.521	R
RU 149F	13.895	V
RU 149F	13.007	R
RU 149G	13.270	V
RU 149G	12.632	R
RU 152	13.464	V
RU 152	13.214	R
RU 152A	14.772	V
RU 152A	14.147	R
RU 152B	15.413	V
RU 152B	14.826	R
RU 152C	12.649	V
RU 152C	12.001	R
RU 152D	11.499	V
RU 152D	10.875	R
RU 152E	12.810	V
RU 152E	12.468	R
RU 152F	14.975	V
RU 152F	14.287	R

are characterised by one or more pixels having anomalously large ADU values) was performed by using a rejection algorithm in `Imcombine`. The algorithm used was `ccdclip` which uses the known characteristics of the CCD (read-noise and gain) to calculate an expected sigma value for each pixel by using the median of the pixel values (excluding the maximum and minimum pixel values). The expected sigma (per pixel) is given by

$$\sigma = \left(\frac{rn}{g}\right)^2 + \frac{\langle I \rangle}{g} + \sqrt{(s \langle I \rangle)^2}, \quad (2.3)$$

where

rn = read-out noise,

g = gain,

$\langle I \rangle$ = true pixel value (approximated using the median of un-rejected pixels),

s = sensitivity noise (set to 0 if unknown).

Pixels were rejected if their values exceeded 3σ above or below the σ values calculated above. This proved to be effective in removing cosmic ray strikes. The zero point (or sky level) of each individual image was adjusted (by adding a constant value to each pixel) so that the mode of each image (prior to combining) was the same. This is required since the combining operation is based on the deviation from the median of the images (the zero point of each image will vary due to the Poisson nature of the arrival of photons and differences in airmass). The images were then combined using the median of the pixel values in each image, excluding rejected pixels (ie. the median of spatially coincident pixels were mapped to single pixels in the combined frame). The final 'master' V and R images of the galaxies and the control field have effective exposure times of 900 seconds each, however, they have a greater S/N than the individual frames since the $S/N \sim \sqrt{n}$, where n is the total number of combined frames (Harris 1989). Figure 2.5-2.7 display the trimmed images of HCG 22a, HCG 90c and the control field.



Figure 2.5: HCG 22a.

Since globular cluster candidates are detected as a statistical excess of star-like objects, it is imperative that the seeing for the galaxy and control fields be the same. Seeing affects both object detection and classification in the sense that a decrease of the seeing disk reduces crowding effects and also improves the ability to reliably distinguish between star-like objects and small, faint galaxies. If the seeing varies greatly from frame to frame, all fields must have their effective seeing altered to match the 'worst-seeing' image. This can be done by convolving the fields with a Gaussian function so that the full-width-half-maximum (FWMH) of star-like objects are the same.

Table 2.9 lists the estimated seeing for the galaxy and control frames. Since the seeing is approximately the same for all frames, no attempt was made to alter the seeing in any of the frames.



Figure 2.6: HCG90c (slightly right of centre)

Table 2.9: Seeing log for combined images.

Field	Passband	Seeing (")
HCG 22a	V	0.87
	R	0.87
HCG 90c	V	0.98
	R	0.98
Control	V	0.93
	R	0.96



Figure 2.7: Control field.

2.5 Galaxy Light Removal

At the distances of these galaxies (> 10 Mpc) and with the typical seeing of the data, individual globular clusters are unresolved and appear as an apparent excess of stellar-like objects around their parent galaxy. Thus in order to detect as many of the individual GCs as possible, the large-scale light distribution of the parent galaxy must first be removed.

The galaxy light from HCG 22a and HCG 90c was removed using the STSDAS package in IRAF. The routine `ellipse` was used to fit elliptical isophotes over the individual galaxies and `bmodel` was used to construct a smooth model of the galaxy light. This model was then subtracted from the individual galaxy frames.

For HCG 22a, the isophotal fitting (which uses the method of Jedrzejewski 1987) was carried out to a radius of $\sim 2'$ (~ 21 kpc assuming $H_0 = 75$ km/s/Mpc). The centre, ellipticity and the position angle of the fitting parameters were allowed to vary out to the outer radius given above. Since the fitting process was carried out to a radius where the surface brightness was approaching the sky value, the subtraction of the galaxy model, created by `bmodel`, left no artifacts of the subtraction process and thus the light from the galaxy was effectively removed.

With the removal of the galaxy light, the well-known central dust lane in HCG 22a (Franx, Illingworth & Heckman, 1989) was apparent, as well as a much more extended, diffuse dust lane (see Figure 2.8). In order to remove the light from the extended dust lane feature as much as possible, the galaxy image was median filtered using the routines `Rmedian` and `Median`. The `Rmedian` routine uses the fast ring median filter described by Secker (1995). A circular annulus of inner radius 6.36 pixels and an outer radius of 7.36 pixels was used to remove structures with a scale length < 6.36 pixels. The ring median filter replaces the value of the central pixel with the weighted median of the pixels contained within the defined annulus. Thus all star-like features are replaced by the value of the local background. The smoothed

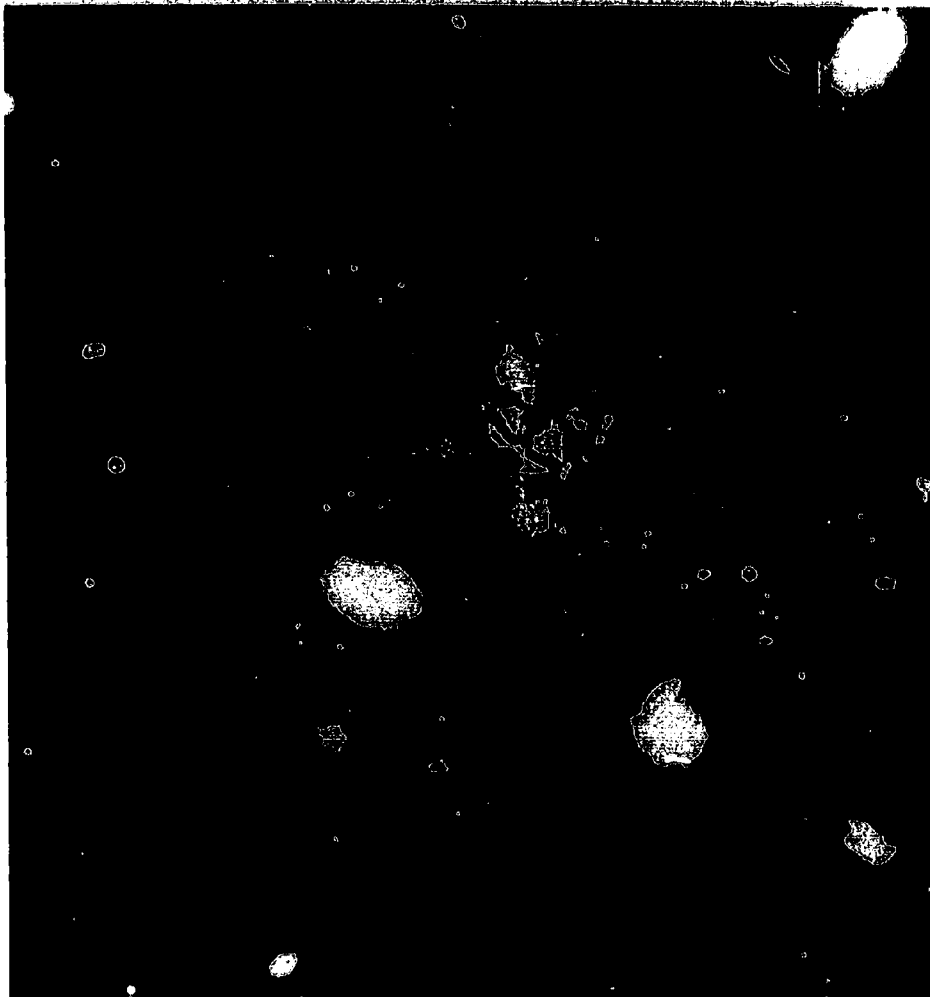


Figure 2.8: STSDAS/Bmodel subtracted image of HCG 22a.

image produced by `Rmedian` was then subtracted from the galaxy image, which helped to remove some of the large-scale light from the diffuse dust lane.

A second median filtering was applied to the resultant galaxy image using the routine `Median`. `Median` uses a rectangular sliding window of dimensions X and Y to remove small-scale structures by replacing the central pixel value by the median of the pixel values in the rectangular filter. For HCG 22a, a rectangular filter of dimension 10×10 pixels was used and the resultant image produced by `Median` was subtracted from the galaxy image. Finally, a constant was added to the median-filtered-subtracted galaxy image in order to restore the background level to its original value. The above procedure was applied equally to both the V and R image. Inspection of the

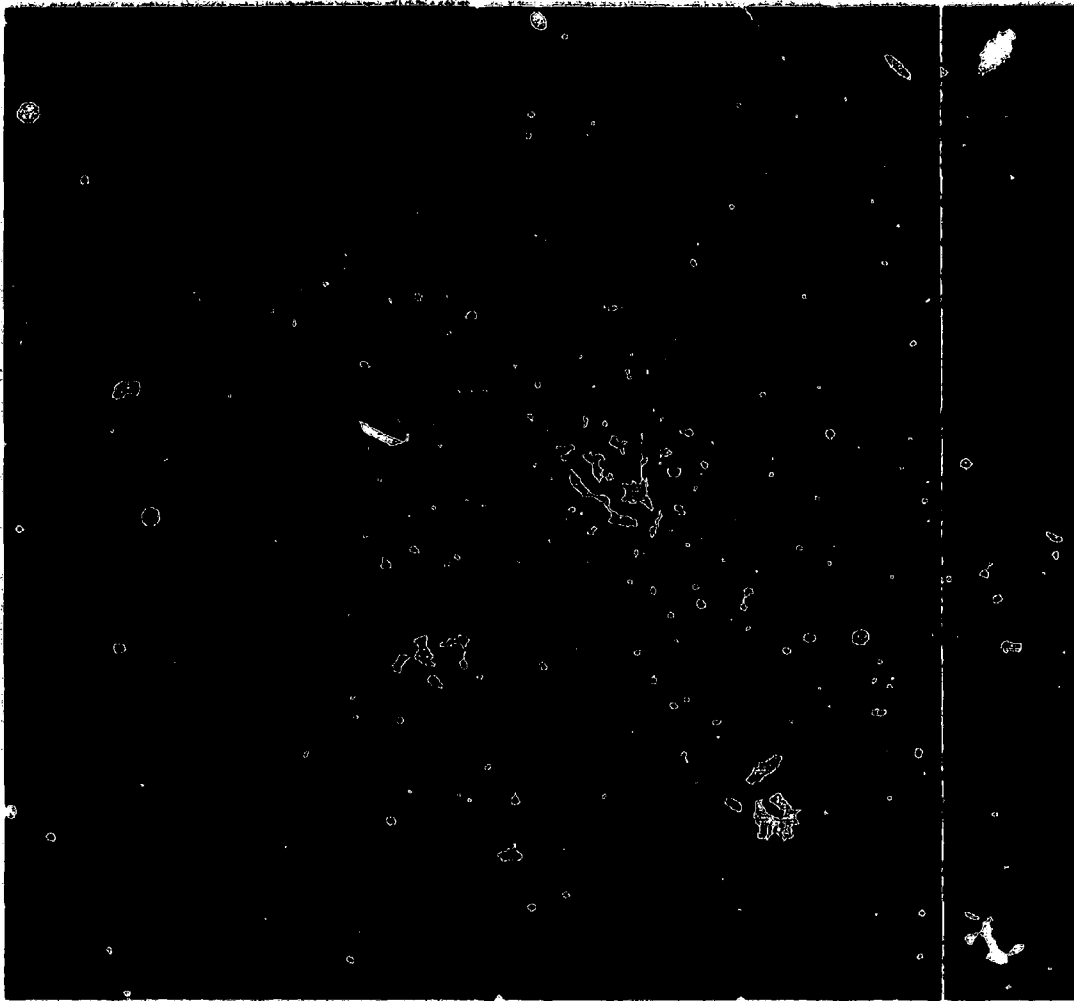


Figure 2.9: Median filtered subtracted image of HCG 22a.

galaxy image clearly shows an excess of stellar-like objects surrounding HCG 22a (see Figure 2.9).

For HCG 90c, the STSDAS routine `Ellipse` was used to fit elliptical isophotes to a radius of $\sim 0.5'$ (~ 5 kpc assuming $H_0 = 75$ km/s/Mpc) from the galaxy centre. The isophote fitting was not carried out to a larger radius due to the increasing non-elliptical nature of the isophotes with radius. This effect is most likely due to the interaction with HCG 90d, which is clearly being disrupted (Hickson 1994). The isophote fitting parameters, centre, ellipticity and position angle, were allowed to vary out to the outer fitting radius. The galaxy model created by `Bmodel` was next subtracted from the galaxy and, since the fitting was not carried out to a radius where

the galaxy light reaches the background, a small circular artifact remained after the subtraction process (see Figure 2.10).

In order to remove the remaining galaxy light near the centre, where `Bmodel` often has trouble, the ring median filter was applied in the same way as that used for HCG 22a. The resultant median-filtered-subtracted image did not require a second filtering process using a rectangular filter. A constant value was added to the galaxy image in order to restore the original background level. The galaxy removal process was applied equally to both the V and R image. Inspection of the galaxy image clearly shows an excess of stellar objects surrounding HCG 90c (see Figure 2.10).

Since the control field did not contain any bright galaxies, it was not necessary to median filter the image.

2.6 FOCAS

The detection and classification of objects in the program frames was performed using FOCAS (Faint Object Classification and Analysis System) within the IRAF environment (Jarvis & Tyson 1981; Valdes 1993). The goal of using FOCAS is to construct a list of star-like objects for both the galaxy frames and the control field. FOCAS has been shown to be more suitable than the DAOPHOT routine `Daofind` in detecting extended objects of low surface brightness (as well as stellar objects), except in very crowded stellar fields (Neuschaefer et al. 1995). However, only one previous study to date has used FOCAS to detect globular cluster candidates around another galaxy (Thompson & Valdes 1987).

The first step in using FOCAS is to set the detection parameters using the routine `Setcat`. For this study, a detection threshold of 2.5σ above background was used, thus any object whose pixel value is greater than 2.5σ above background will be detected. The detection threshold below background can also be defined and this was given the value of 10σ (ie. no object was detected below background). The background sky σ can be automatically determined or defined by the user. Automatic sky determination

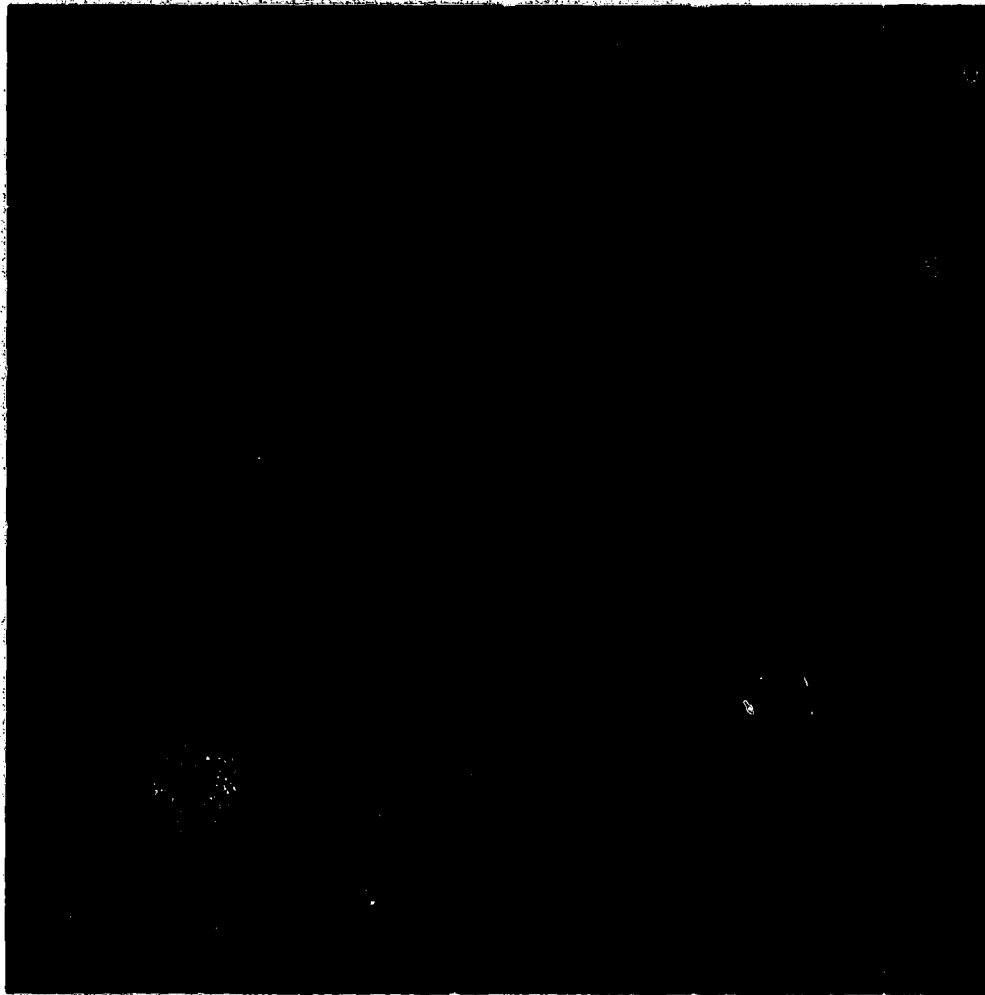


Figure 2.10: Median filtered subtracted image of HCG 90c.

Table 2.10: Classification Rules

Scales	Class
0.10-0.60	noise
0.61-1.20	star
1.21-10.00	galaxy
10.01-100.00	diffuse

is done by examining the first few lines of the input image. However this procedure is risky since any bright sources near the edge of the frame can bias the value calculated for the sky σ . Experimentation showed that the sky σ was best determined manually and for this purpose, the DAOPHOT routine, *Daoedit*, was used.

Besides the σ values, a detection filter size must be supplied by the user. The *Detect* routine uses the detector filter to assign a weighted value to individual pixels from the values of the pixels within the detection filter. Experimentation showed that the use of a delta function (ie. no detection filter) maximized the sensitivity for object detection.

The final important parameter that must be specified is the classification rules. FOCAS uses a resolution classifier (Valdes 1982) to classify detected objects by comparing a series of templates constructed from the point spread function of a number of point sources (isolated, unsaturated, bright stars). The PSF templates are scaled to various sizes and the template that best matches a resolved object is given the classification set by the scale values. Thus an object whose scale value is near that of the PSF would be classified as a 'star' while those with a broader scale may be classified as 'galaxy' or 'diffuse'. The classification rules used for this study are similar to those that were used by Hintzen, Romanishin & Valdes (1991) and Röttgering et al. (1995), who showed that these classification parameters provide a sensitive discrimination between noise, stars, galaxies, and diffuse objects (extended light structures). Table 2.10 list the classification rules used for this study.

After running the *Setcat* routine, the next step is to use *Detect* which classifies a

positive detection as an object that has a minimum number of contiguous pixels (set by the user) with values greater than the threshold σ . The minimum area was set at six pixels since the seeing is ≈ 3 pixels (FWHM) and any detected object not covering six pixels must be 'noise'. The next step is to use the **Sky** routine which generates a local sky value around each object using a square annulus. Next, the routine **Evaluate** determines most of the object parameters (such as shape measurements, photometry, etc.) but does not classify objects. The next step is to use **Splits** which separates multiple objects into two or more objects by increasing the detection threshold and examine objects for disconnected regions (satisfying the minimum area criteria). This process is repeated until no further objects are detected. After running the **Splits** routine, a PSF (point spread function) template is constructed using the routine **Autopsf** which selects a user defined number of stars in which to build a PSF model. The user defined values used in this study for **Autopsf** were; minimum number of stars = 10, σ constraint in the scatter of template size = 0.05, and the size of the PSF template = 11×11 pixels.

The final FOCAS routine needed to classify image objects is the routine **Resolution**. **Resolution** classifies the detected objects by broadening or narrowing the model PSF in order to determine a 'best-fit' to the detected object. The class assigned to this object is defined by the classification rules using **Setcat** (see above).

Once FOCAS had been used to construct a catalog of detected and classified objects, the object list was culled of all objects that were non-stellar, saturated, and those that were located at the edge of the field. The above steps were repeated for all frames, in both V and R, using identical parameters (except for the different sky σ).

The final step was to use the **Match** routine (Valdes et al. 1995) to construct a catalog of objects that were found in both the V and R passbands. By including only objects that were matched in both passband, the probability of a false detection (such as a cluster of pixels with higher than average ADU values) is greatly reduced.

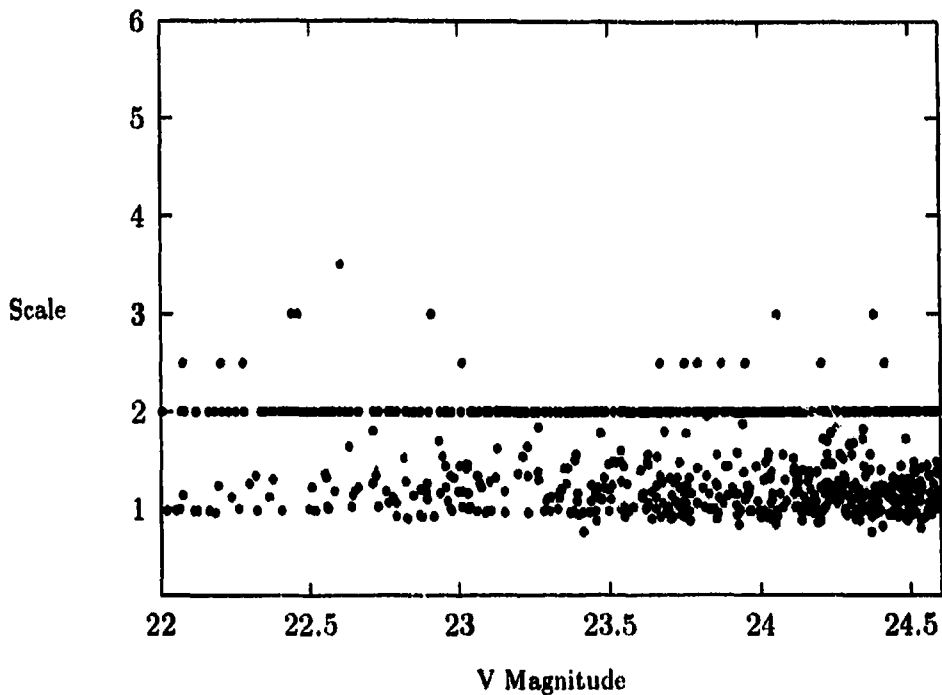


Figure 2.11: Plot of FOCAS scale parameter versus V magnitude for HCG 22a.

Figures 2.11–2.13 show plots of the FOCAS ‘scale’ parameter versus V magnitude for both galaxy fields and the control field. Objects plotted include only those that were detected and classified as ‘star’ and ‘galaxy’ down to the limiting magnitude of $V=24.6$ (classification rules are summarized in Table 2.10). From the figures, it appears that FOCAS has equally applied its classification criteria to detected objects in all three fields. However, a clear separation does not exist for stars and galaxies and thus FOCAS seems to be unable to accurately classify faint background galaxies which mimic star-like objects (a problem for all classification programs).

2.7 Instrumental Magnitudes

All instrumental magnitudes were derived using the IRAF version of DAOPHOT. A brief summary of the required processing steps include: using the routine **Photo** to obtain aperture magnitudes, building a PSF model using **Pstselect**, **Psf**, **Nstar** and **Substar**, and finally calculating PSF magnitudes using **Peak**.

While the standard star magnitudes were measured using a large aperture of 15

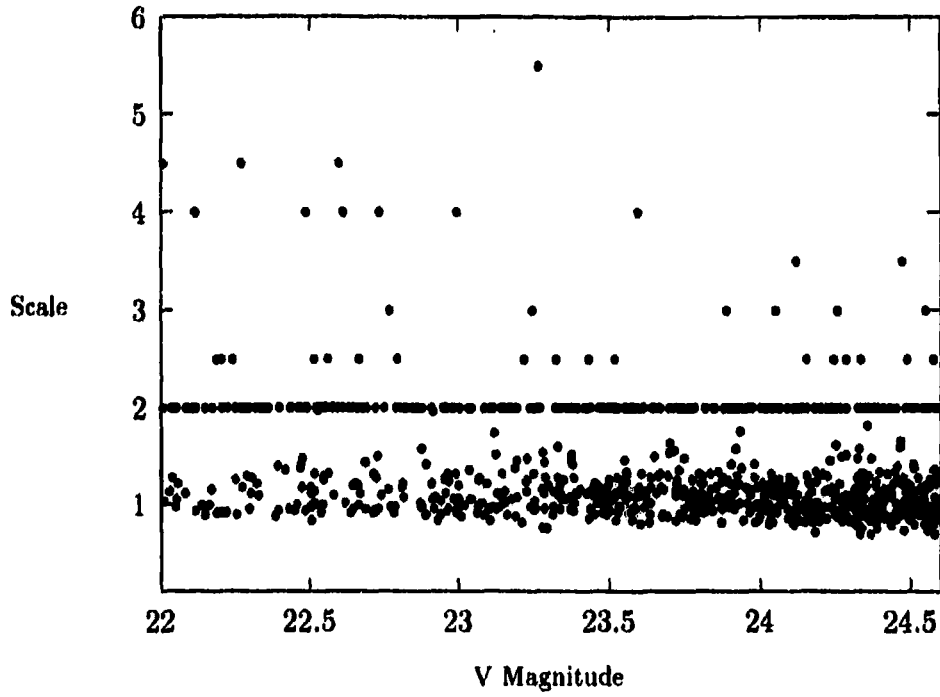


Figure 2.12: Plot of FOCAS scale parameter versus V magnitude for HCG 90c.

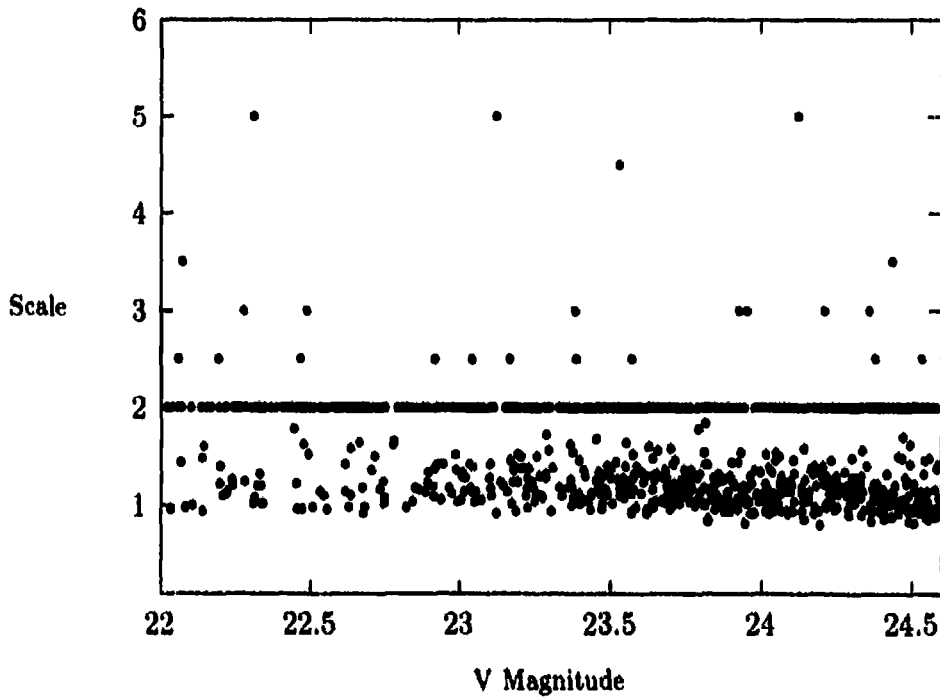


Figure 2.13: Plot of FOCAS scale parameter versus V magnitude for the control field.

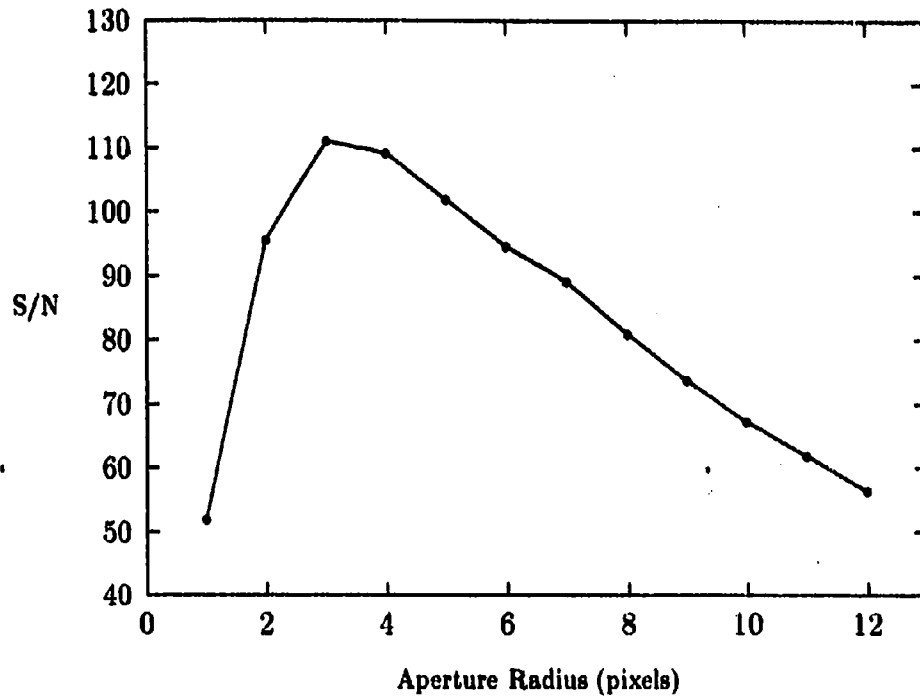


Figure 2.14: Plot of S/N versus aperture radius for a $V=14.2$ point source. The S/N reaches a maximum at $\sim FWHM$ (3 pixels) of the stellar profile (data taken from Howell 1989).

pixels in radius, the program objects (globular cluster candidates and star-like objects in the control field) had to be measured using a smaller size aperture. This is because the program objects are found in fields which are significantly more crowded than the standard stars, and hence an aperture of 15 pixels in radius would most likely enclose the light from several stars. Since the program objects are generally very faint ($V=22$ to 25 magnitude) the 'best' aperture size to use is one which maximizes the signal-to-noise ratio. Howell (1989) has shown that the S/N ratio reaches a maximum at an aperture radius that is approximately equal to the FWHM of the source object. For radii smaller than the FWHM, the S/N ratio decreases due to the decrease in the number of source pixels and hence increasing the noise. The S/N decreases for radii larger than the FWHM due to the increase of noisy pixels within the measuring aperture (see Figure 2.14).

Since the FWHM of the program objects was ~ 3 pixels, an aperture radius of 3 pixels was used to measure aperture magnitudes using Phot. The difference in

aperture size, used to measure the standard stars and the program objects, must be taken into account. This is done by applying an 'aperture correction' to the measured magnitudes of the program objects (see below).

In order to calculate PSF magnitudes for the program objects, a model PSF was constructed. The routine `Pstselect` was used to compile a list of 25 bright, star-like objects in the median filtered subtracted galaxy frames and the control field. The routine `Psf` was used to construct a model PSF from the selected sample of stars. Next, `Nstar` and `Substar` were used to subtract the PSF stars and the resultant images were examined for any remaining subtraction artifacts. Once a 'clean' subtraction was achieved, the PSF model was used by `Peak` to derive PSF magnitudes with a fitting radius of 3 pixels.

In order to convert PSF magnitudes to instrumental magnitudes (those that are entered directly into the transformation equations) an aperture correction must be applied. An aperture correction is a magnitude value that is added to the PSF magnitudes in order to compensate for the fact that the magnitudes of the standard stars were measured through an aperture much larger than that used for the program objects. Aperture corrections were calculated using the PHOTCAL routine `Mkapfile`, which uses the program DAOGROW to compute the required values (Stetson 1990). The general procedure was to perform aperture photometry, using a series of aperture sizes from 3 to 15 pixels in radius, on several isolated, unsaturated, bright stars on *individual* frames (ie. on images before they were combined and median filtered). The reasons for using individual frames are: 1) the median filtering process cuts off the faint extended outer wings of the star-like objects (and hence a wrong aperture correction would be calculated)³; and 2) the mean airmass is better defined for a single exposure as compared to a series of combined exposures (Harris 1995).

Five bright, isolated stars were located on the galaxy and control field frames and a

³Since the size of the ring median filter was ~ 7 pixels in radius, the inner part of the stellar profiles are unaffected by the median filtering and magnitudes derived by fitting a PSF to a radius of three pixels are accurate.

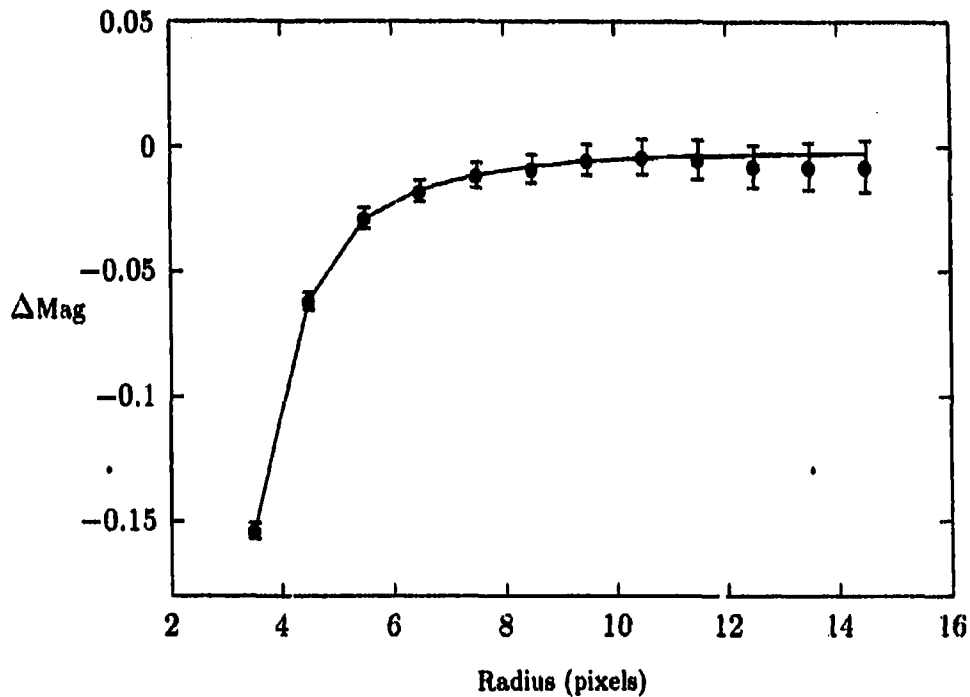


Figure 2.15: Plot of the adopted curve-of-growth profile for a single R-band image of HCG 90c. The data points are the observational data from several bright, isolated stars.

series of aperture magnitudes were obtained per frame. `Mkapfile` computes an observational and theoretical curve-of-growth (magnitude differences between successive apertures plotted against radius) and constructs a 'best-fit' curve using a weighted average of the observed and theoretical curves. The observational curve is given more weight for smaller radii (observational S/N is higher), and the theoretical curve for larger radii (where the observational data are noisier). The aperture correction is calculated by integrating the adopted curve from an inner radius of 3 pixels to an outer radius of 15 pixels. Figure 2.15 shows a plot of the adopted curve-of-growth for a single R image of HCG 90c.

Aperture corrections for the combined frames were calculated using the weighted mean of the individual aperture corrections. Table 2.11 shows the aperture corrections used for the galaxy and control fields.

Table 2.11: Aperture Correction

Field	Filter	Aperture Correction (magnitude)
HCG 22a	V	-0.155
HCG 22a	R	-0.233
HCG 90c	V	-0.248
HCG 90c	R	-0.219
Control	V	-0.228
Control	R	-0.245

2.8 Standard Magnitudes

Standard magnitudes for the program objects were calculated using the derived transformation equations. The PHOTCAL routine `Mkobsfile` was used to construct a list of objects that had magnitude measurements in both V and R passbands. The PHOTCAL routine `Inverfit` was then used to derive instrumental magnitudes by adding together the aperture correction and the measured psf magnitudes. `Inverfit` was then used to calculate the standard V and R magnitudes using the transformation equations.

Chapter 3

Data Analysis

3.1 Completeness Tests

Since the globular cluster populations of HCG 22a and HCG 90c are detected only at very faint magnitudes ($V \sim 25$), the probability of detecting an object as a function of magnitude must be determined as accurately as possible. A 'completeness function' was calculated by adding artificial stars to the galaxy and control field frames and re-running the FOCAS routines. The fraction of detected stars, as a function of magnitude, could then be used to derive the completeness limits. The DAOPHOT routine `Addstar` uses a model PSF (scaled to various heights) to add stars to an image with a user defined magnitude and location.

For HCG 22a, six artificial stars were added to the final galaxy frame at different locations and with a range in magnitude of 0.2. Only six stars were added (representing $\sim 1.2\%$ of the total number of detected star-like objects) since experimentation showed that the addition of more stars would affect the crowding characteristics of the field and this would in turn adversely affect the completeness function¹. Artificial stars were added to both V and R frames using the same spatial coordinates and with a $V-R=0.4$ (approximately the colour of Milky Way globular clusters; see Peterson 1993). FOCAS was then run *exactly* in the same manner as that used for the program objects, including only keeping objects that were detected in both V and R

¹While running completeness tests for this study, the addition of stars (amounting to only 10% of the total number of program objects) greatly affected the ability of FOCAS to detect and classify objects.

passbands. A total of 169 trials, with six stars each, were carried out with a range in V magnitude from 22–25.2 (in 0.2 magnitude bins). The completeness data for HCG 22a are presented in Table 3.1.

The uncertainties given in Table 3.1 were calculated using equations from Bolte (1989). The variance in the completeness fraction, f , (assuming Poisson and Binomial statistics) is given by

$$\sigma_f^2 = \frac{f(1-f)}{n_{\text{added}}}, \quad (3.1)$$

where

$$f = \frac{n_{\text{recovered}}}{n_{\text{added}}}.$$

The photometric magnitude limit of the data was defined to be the magnitude at which the probability for detecting an object drops to 50% (Harris 1990). For magnitudes fainter than this level the information is much less reliable and all such objects were discarded from further analysis. A cubic spline interpolation function was used to determine that $f = 0.5$ at a V magnitude of 24.9 for the HCG 22a field. A plot of the completeness fraction versus magnitude is given in Figure 3.1. From the figure, it can be seen that the data is nearly 100% complete up to a critical magnitude upon where the completeness function drops rapidly (this behavior is generally seen in other studies).

In addition to determining the completeness function for the field in general, the function of completeness versus radial distance from the centre of the galaxy must also be determined. Since both the noise and the degree of crowding increase toward the centre of the galaxy, incompleteness will vary with radial distance from the galaxy centre. Artificial stars were added at different radii from the galaxy centre and the completeness limit was determined as a function of radial distance. For HCG 22a, it was found that the completeness function drops towards zero for radii less than 70 pixels from the galaxy centre (part of this is due to the presence of a small disk-like feature (related to the central dust lane) at the centre of HCG 22a). All objects found within 70 pixels of the galaxy centre were therefore discarded and this inner region

Table 3.1: Completeness Data For HCG 22a.

V	n_{added}	n_{found}	$f_{\text{completeness}}$	σ_f
22.0-22.2	48	48	1.000	0.000
22.2-22.4	48	48	1.000	0.000
22.4-22.6	48	48	1.000	0.000
22.6-22.8	48	48	1.000	0.000
22.8-23.0	48	48	1.000	0.000
23.0-23.2	48	47	0.979	0.021
23.2-23.4	60	58	0.967	0.023
23.4-23.6	60	59	0.983	0.017
23.6-23.8	66	56	0.848	0.044
23.8-24.0	60	52	0.867	0.044
24.0-24.2	72	68	0.944	0.027
24.2-24.4	72	63	0.875	0.039
24.4-24.6	72	50	0.694	0.054
24.6-24.8	72	46	0.639	0.057
24.8-25.0	72	40	0.555	0.058
25.0-25.2	72	15	0.208	0.048

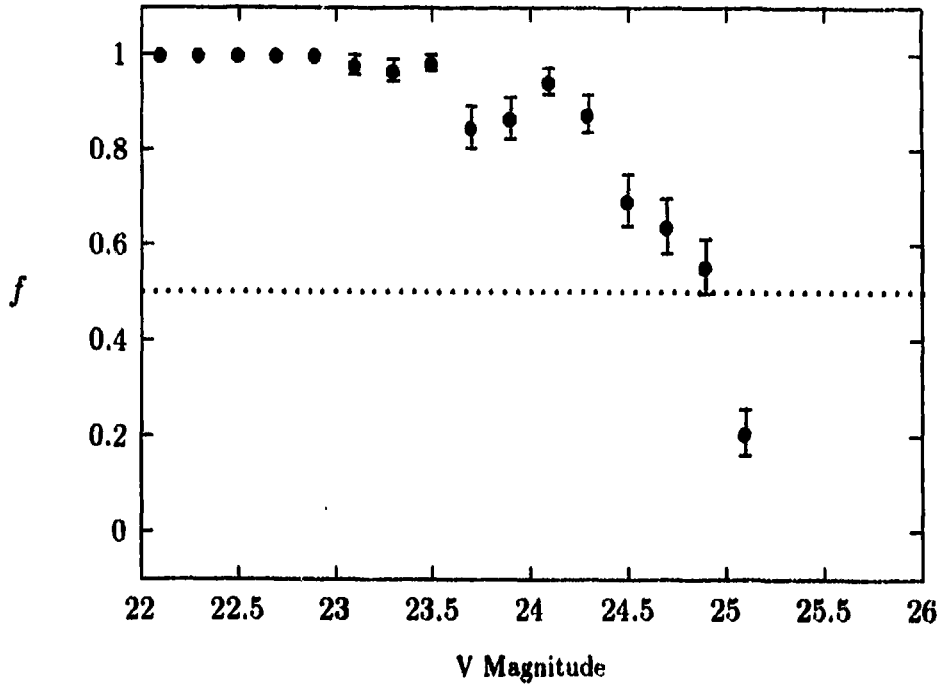


Figure 3.1: Completeness function for HCG 22a. Data points represent the fraction of recovered artificial stars for each magnitude bin. The value of f reaches 0.5 at $V=24.9$ magnitude.

Table 3.2: Completeness Data For HCG 90c.

V	n_{added}	n_{found}	$f_{\text{completeness}}$	σ_f
22.0-22.2	40	40	1.000	0.000
22.2-22.4	40	40	1.000	0.000
22.4-22.6	40	40	1.000	0.000
22.6-22.8	40	40	1.000	0.000
22.8-23.0	48	48	1.000	0.000
23.0-23.2	64	64	1.000	0.000
23.2-23.4	64	64	1.000	0.000
23.4-23.6	64	64	1.000	0.000
23.6-23.8	64	64	1.000	0.000
23.8-24.0	64	64	1.000	0.000
24.0-24.2	64	64	1.000	0.000
24.2-24.4	80	75	0.938	0.027
24.4-24.6	80	70	0.875	0.037
24.6-24.8	80	54	0.675	0.052
24.8-25.0	80	16	0.200	0.045
25.0-25.2	64	0	0.000	0.000

was not used in further analysis. For radii greater than 70 pixels, the completeness function is the same over the whole field.

For HCG 90c, eight artificial stars were added to the galaxy field per trial (representing $\sim 1.2\%$ of the total number of detected star-like objects in the unmasked area). The completeness tests were run in the same way as for HCG 22a with a total number of 127 trials performed. The completeness limit of $f = 0.5$ was determined to be 24.8 V magnitude. Table 3.2 lists the completeness data for HCG 90c and Figure 3.2 presents the completeness function. The radial dependence of the completeness function was calculated in the same manner as for HCG 22a. Tests show that the cutoff in radius from the centre of HCG 90c is 60 pixels and thus, all objects found within this area were discarded.

For the control field, five artificial stars were added to the field ($\sim 1.2\%$ of the total number of detected star-like objects) and a total of 192 trials were performed. The completeness limit of the data was determined to be 24.6 V magnitude. Table 3.3 lists the completeness data for the control field and Figure 3.3 displays the completeness

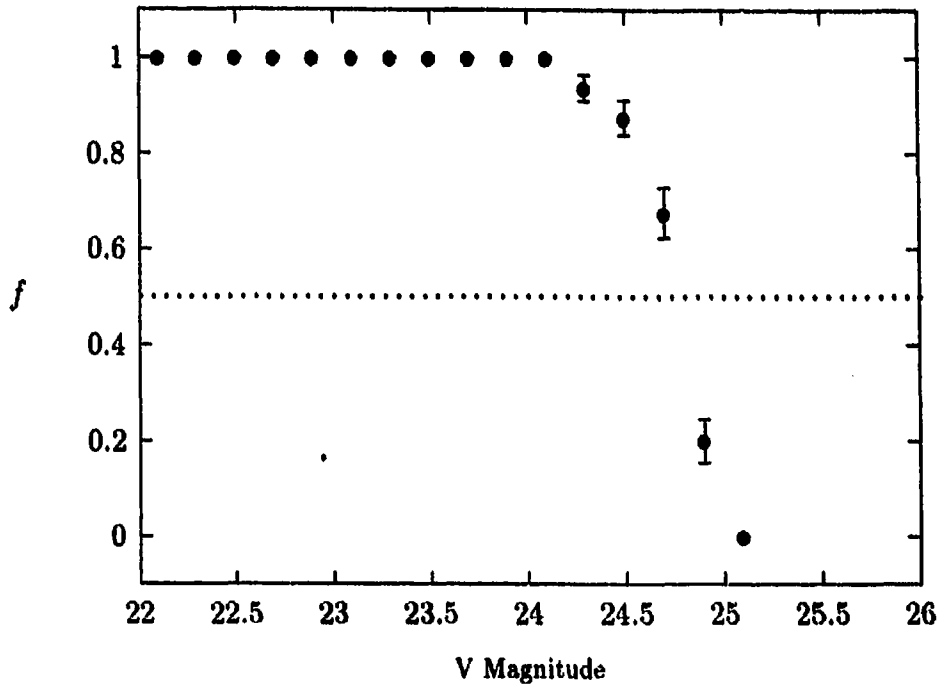


Figure 3.2: Completeness function for HCG 90c. Data points represent the fraction of recovered artificial stars for each magnitude bin. The value of f reaches 0.5 at $V=24.8$ magnitude.

function.

3.2 Final Object List

The detection of globular cluster candidates can be improved using criteria (such as magnitude, colour and shape parameters) which are characteristic of globular clusters in general. Since *both* galaxy fields must be compared to the number of objects detected in the control field, all program objects with magnitudes fainter than $V=24.6$ were rejected, as this was the completeness limit of the control field. Also, at the distance of HCG 22a and HCG 90c, the number of globular clusters brighter than $V=22$ magnitude is negligible and hence all objects brighter than this limit were removed from the object lists. Besides the magnitude criteria, all objects that lie within the masked out regions of the field (such as the inner part of HCG 22a and HCG 90c, as well as regions containing other galaxies) were eliminated from the object lists. In order to improve the S/N of detected globular clusters over background galaxies,

Table 3.3: Completeness Data For Control Field.

V	n_{added}	n_{found}	$f_{completeness}$	σ_f
22.0-22.2	45	45	1.000	0.000
22.2-22.4	45	45	1.000	0.000
22.4-22.6	45	45	1.000	0.000
22.6-22.8	45	45	1.000	0.000
22.8-23.0	45	45	1.000	0.000
23.0-23.2	45	45	1.000	0.000
23.2-23.4	60	60	1.000	0.000
23.4-23.6	60	60	1.000	0.000
23.6-23.8	60	60	1.000	0.000
23.8-24.0	80	80	1.000	0.000
24.0-24.2	80	80	1.000	0.000
24.2-24.4	80	78	0.975	0.017
24.4-24.6	80	68	0.850	0.040
24.6-24.8	80	26	0.325	0.052
24.8-25.0	60	12	0.200	0.052
25.0-25.2	50	9	0.180	0.054

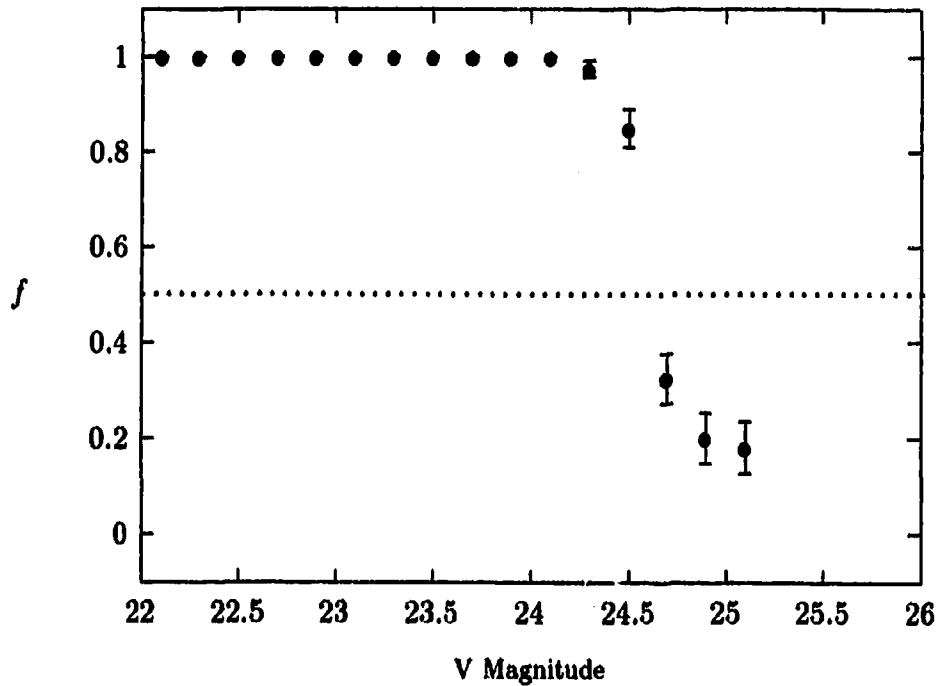


Figure 3.3: Completeness function for the control field. Data points represent the fraction of recovered artificial stars for each magnitude bin. The value of f reaches 0.5 at $V=24.6$ magnitude.

all objects detected more than $2.13'$ (≈ 22.4 kpc assuming $H_0 = 75$ km/s/Mpc) from the centre of HCG 22a were also discarded since at this radius the density of globular cluster candidates becomes low (see section 4.2). For HCG 90c, the corresponding radius is $\sim 2.58'$ or ≈ 24 kpc (see section 4.3) thus all objects further away from the galaxy centre were removed from the object list.

A final cut to the data was made in terms of V-R colour of the program objects. Since the total number of objects is small, a large range in V-R was permitted. Objects having colour in the range of $0.0 \leq V - R \leq 1.2$ were included in the final list. A plot of V versus V-R, for HCG 22a, HCG 90c and the control field is given in Figure 3.4-3.6. From these figures it is clear that the colours of objects in the galaxy fields are different from the objects in the control field in the sense that the galaxy objects generally lie in a more restricted range of V-R than the objects in the control field. This is consistent with the idea that the majority of objects in the galaxy field are globular clusters and hence are not detected in the control field. Tables listing the photometric properties of the globular cluster candidates in HCG 22a and HCG 90c are given in appendix A and B. Figures 3.7 and 3.8 show the spatial distribution of the globular cluster candidates for HCG 22a and HCG 90c, out to the radial limits given above. The masked central region for each galaxy is also displayed.

3.3 Photometric Errors

Errors in the photometry of the globular cluster candidates are plotted in Figure 3.9 and 3.10. The standard deviation, σ , of the individual globular cluster candidates were determined by the PHOTCAL package. An examination of the figures indicates that the standard deviation increases with increasing magnitude and that $\sigma_V \approx 0.1$ at the cutoff limit of 24.6 magnitude for both HCG 22a and HCG 90c.

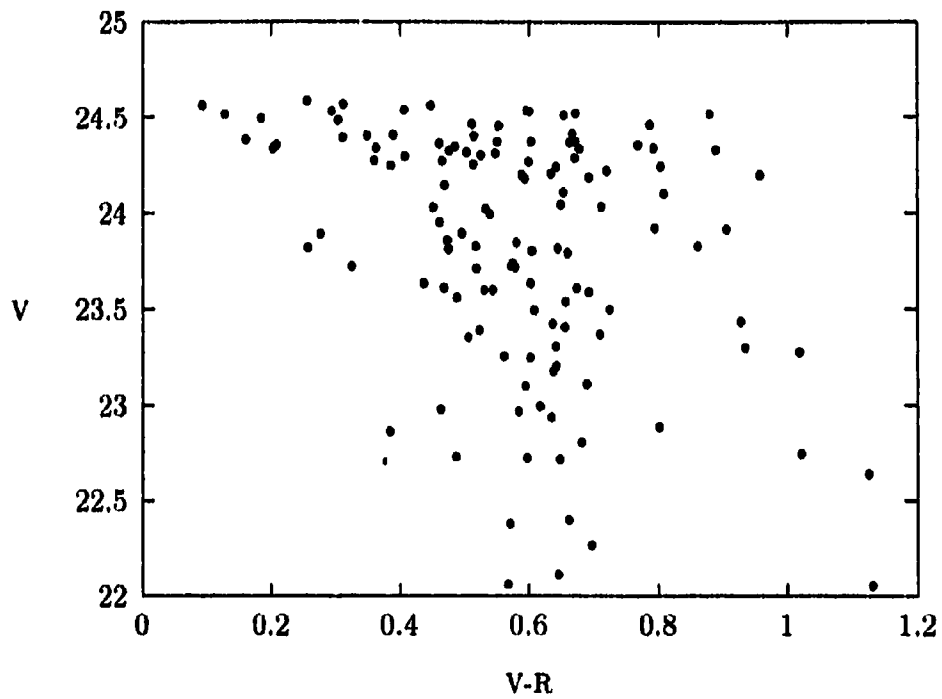


Figure 3.4: Colour-magnitude plot of the globular cluster candidates surrounding HCG 22a. Note the concentration of objects near $V-R \approx 0.6$, which is approximately the colour of Milky Way GCs (Peterson 1993). The increase in scatter towards fainter magnitudes is due to the increase in photometric errors and of faint background galaxies.

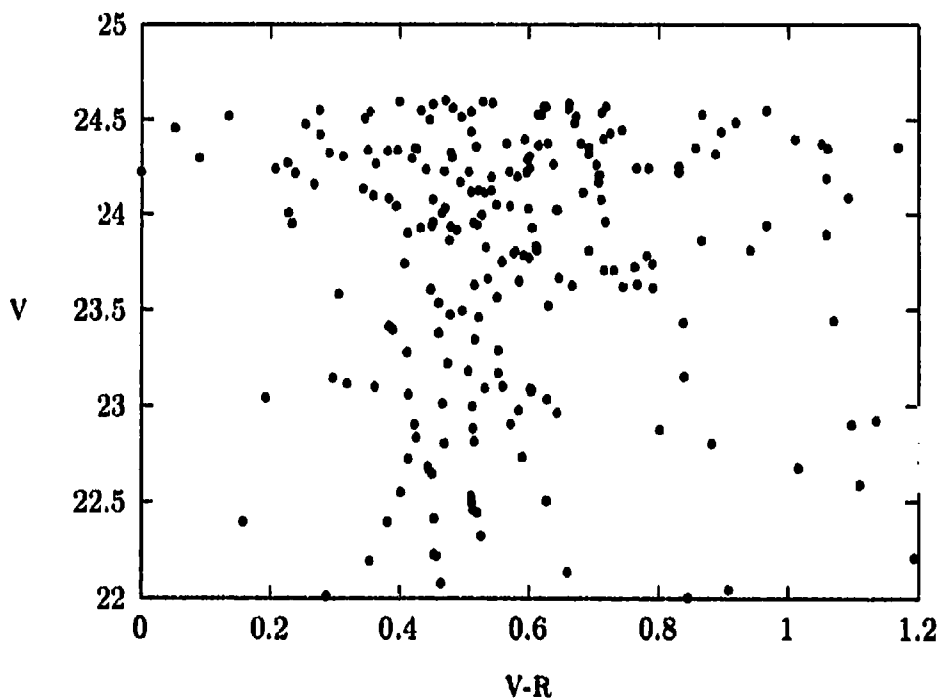


Figure 3.5: Colour-magnitude plot of star-like objects surrounding HCG 90c. Note the concentration of objects near $V-R \approx 0.5$.

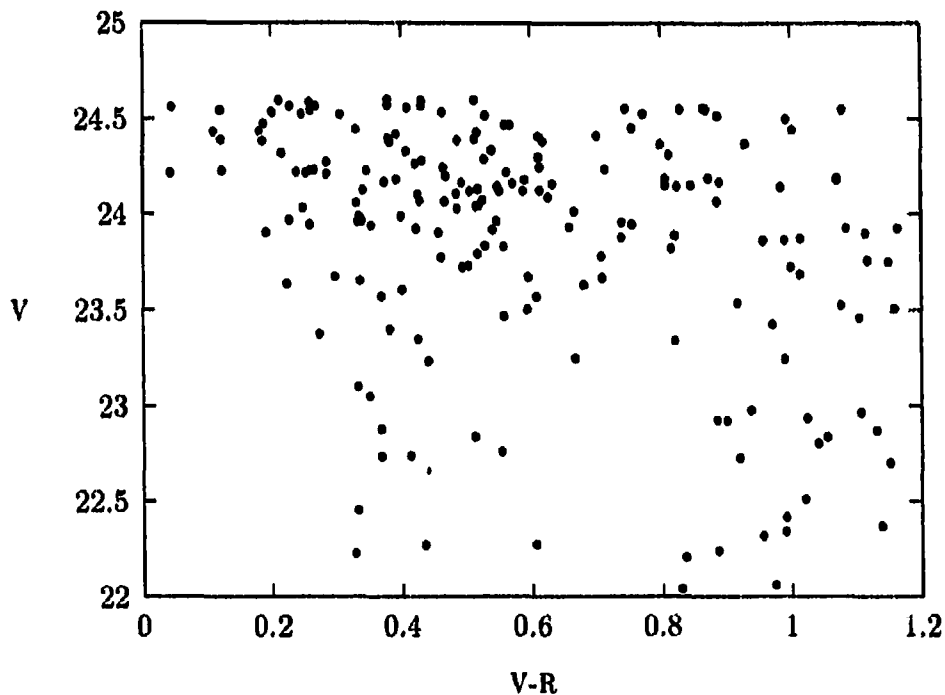


Figure 3.6: Colour-magnitude plot of star-like objects in the control field. Note that the objects appear to be scattered throughout the plot to a greater extent than the colour-magnitude plots for HCG 22a and HCG 90c.

3.3.1 Systematic Errors

Since artificial stars of *known* magnitudes were added to the program frames using *Addstar*, systematic photometric errors can be determined by comparing input and output magnitudes of recovered stars (e.g., Bridges, Hanes & Harris 1991; Butterworth & Harris 1992).

Systematic error, *S.E.*, was defined as

$$S.E. = \frac{\Sigma(V_{add} - V_{found})}{N}, \quad (3.2)$$

where

V_{add} = magnitude of added artificial star,

V_{found} = magnitude of recovered artificial star,

N = total number of stars.

For HCG 22a, the systematic error was determined to be +0.01 magnitudes while for HCG 90c, the error was -0.001 magnitudes. Since the systematic errors are small,

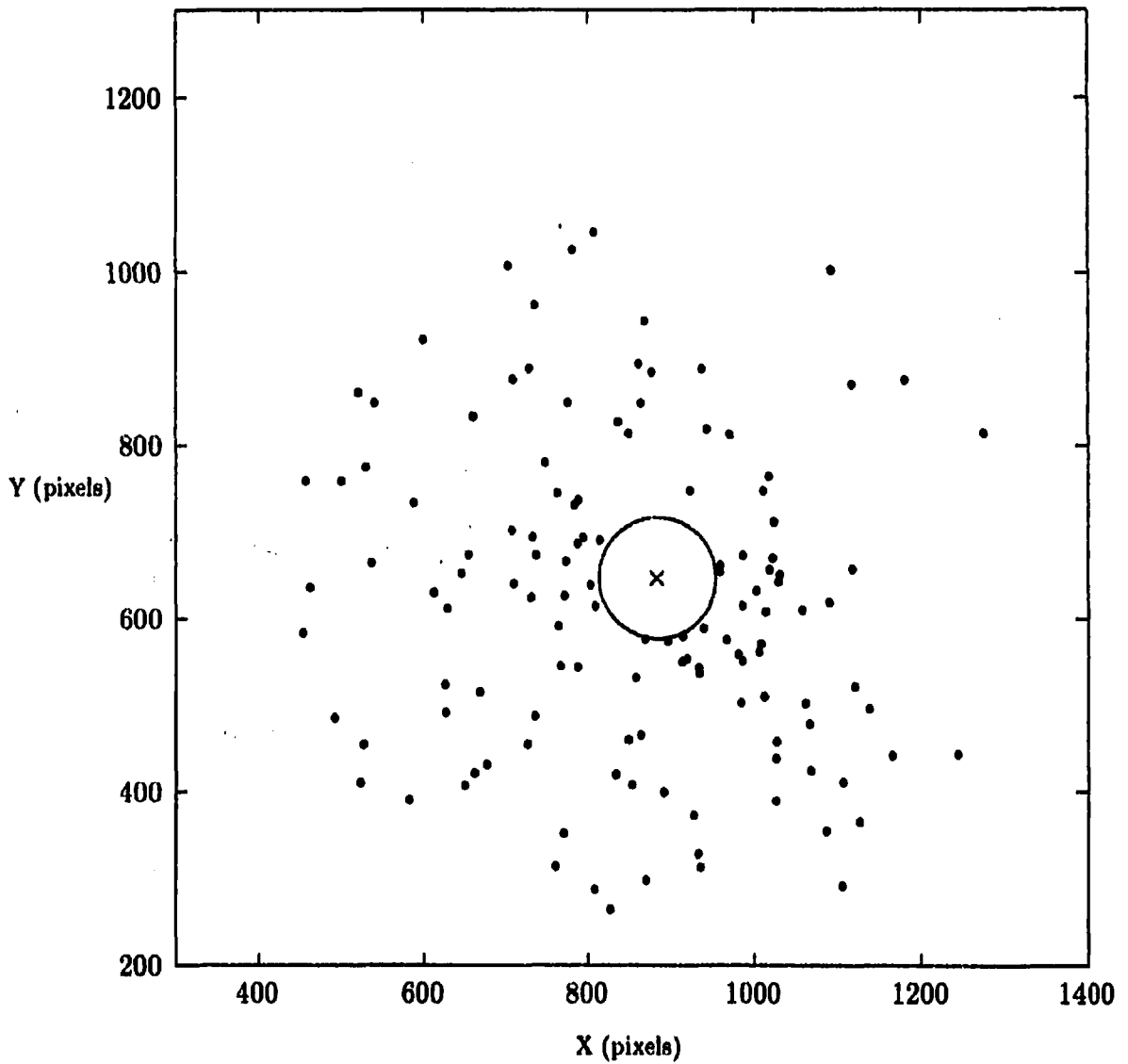


Figure 3.7: Positions of globular cluster candidates with $V \leq 24.6$ surrounding HCG 22a. The central $R = 70$ pixel masked-out region is shown, along with the galaxy centre at $X=885$ and $Y=647$ (marked with an \times). Only those objects having radii $70 \leq R \leq 441$ pixels are shown. Note the concentration of star-like objects around HCG 22a.

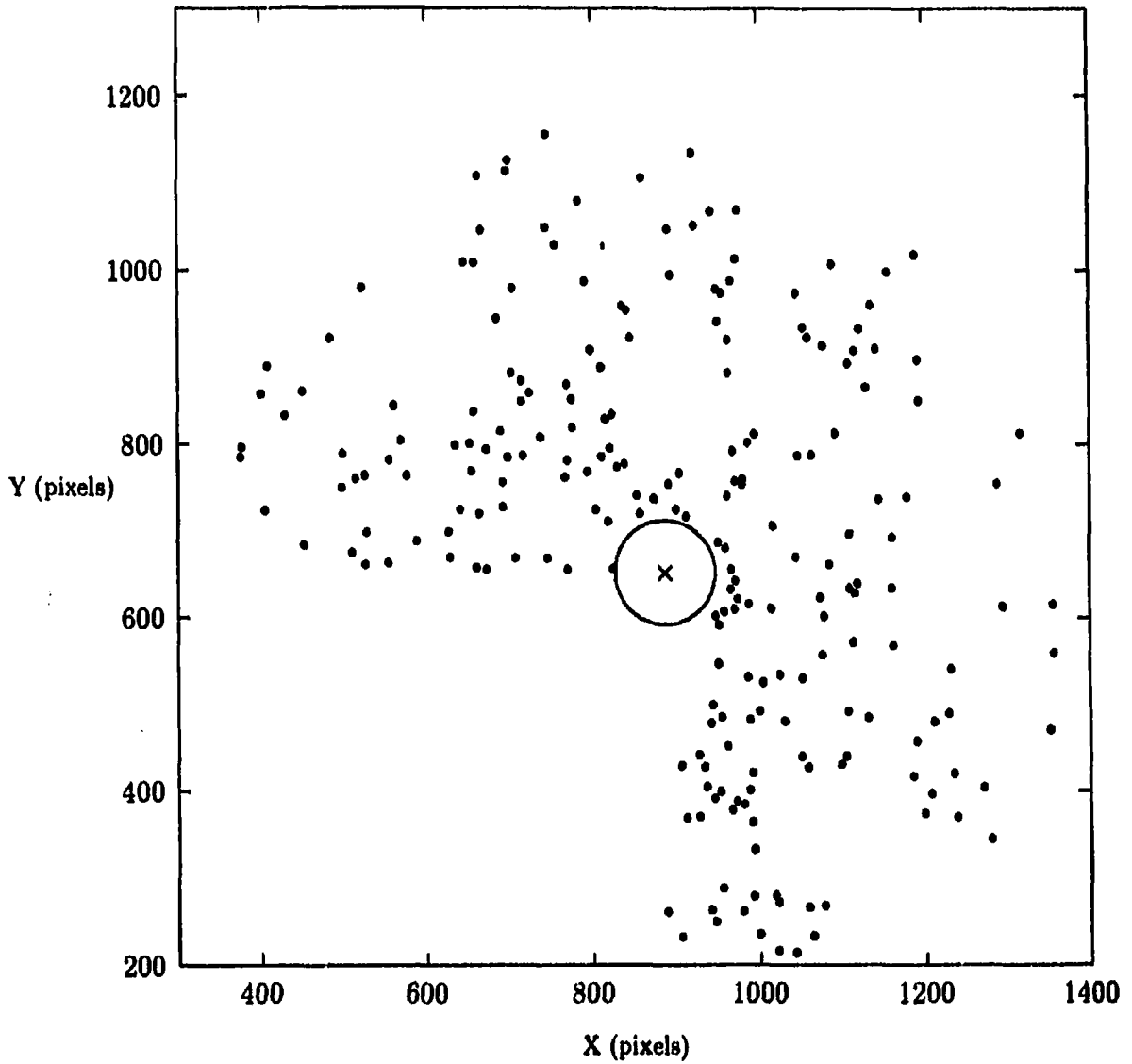


Figure 3.8: Positions of globular cluster candidates with $V \leq 24.6$ surrounding HCG 90c. The central $R = 60$ pixel masked-out region is shown, along with the galaxy centre at $X=887$ and $Y=652$ (marked with an \times). Only those objects having radii $60 \leq R \leq 535$ pixels are shown, excluding the area in the lower left quadrant which was masked out due to the presence of HCG 90b and d (see Figure 2.6). Note the concentration of star-like objects around HCG 90c.

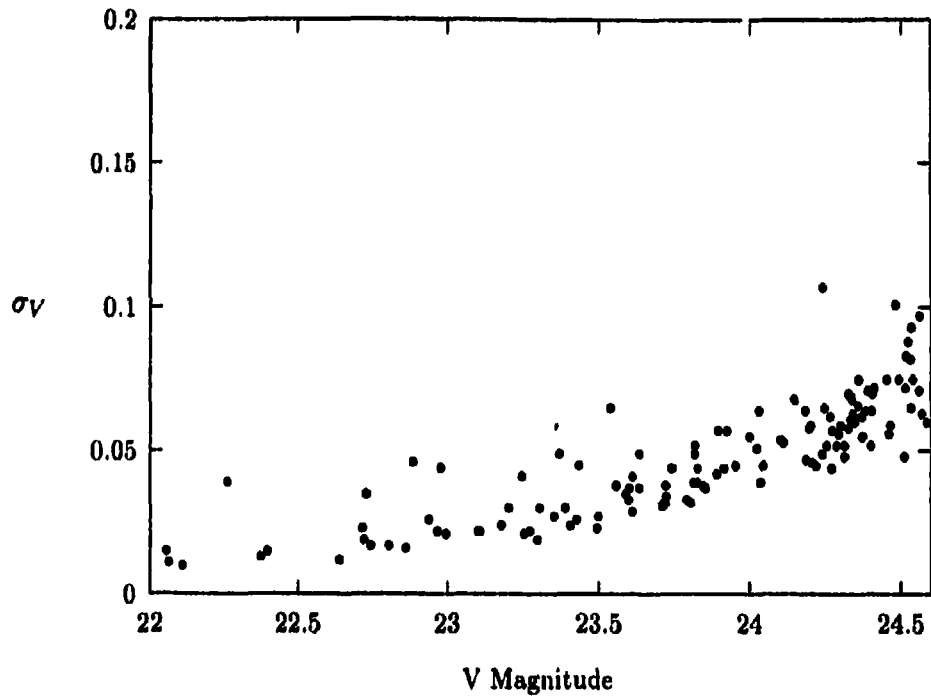


Figure 3.9: A plot of the standard deviation versus V magnitude for the globular cluster candidates in HCG 22a.

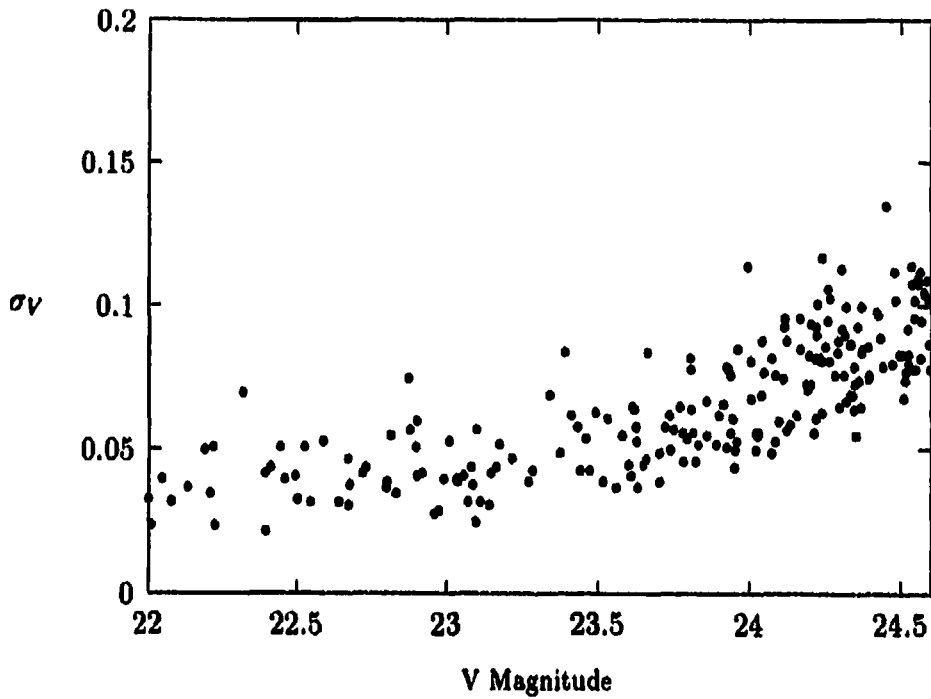


Figure 3.10: A plot of the standard deviation versus V magnitude for the globular cluster candidates in HCG 90c.

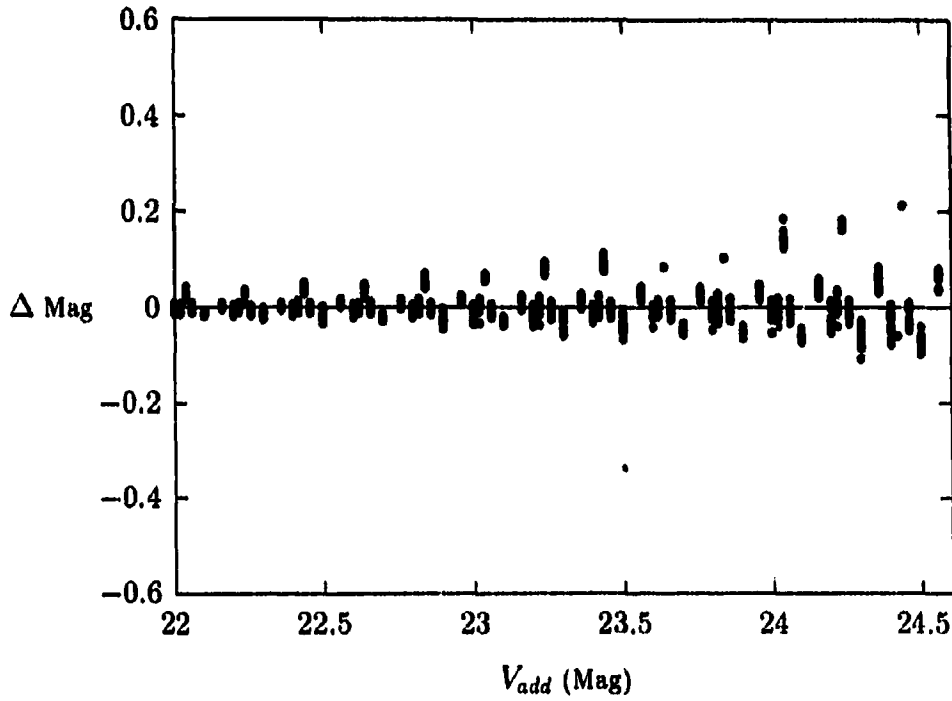


Figure 3.11: Plot of the magnitude difference between added artificial stars (using **Addstar**) and recovered stars, versus V magnitude for added stars in the median filtered HCG 22a field. The scatter about the $\Delta Mag = 0$ axis is defined as the systematic error, which was determined to be negligible for this field.

no correction to the photometric data was undertaken. Figures 3.11 and 3.12 show a plot of the magnitude difference between input artificial stars and recovered artificial stars (for the median filtered galaxy frames). The average of the scatter about the ΔMag axis is defined as the systematic error.

3.3.2 Random Errors

Random photometric errors can also be calculated using the **Addstar** data by examining the standard deviation of the magnitude difference between added and recovered artificial stars. The root-mean-square of the random errors, $\sigma_{v,rms}$, was defined as

$$\sigma_{v,rms}^2 = \frac{\Sigma((V_{add} - V_{found}) - S.E.)^2}{N}, \quad (3.3)$$

where

$S.E.$ = systematic error determined in equation 3.2,

N = total number of added stars.

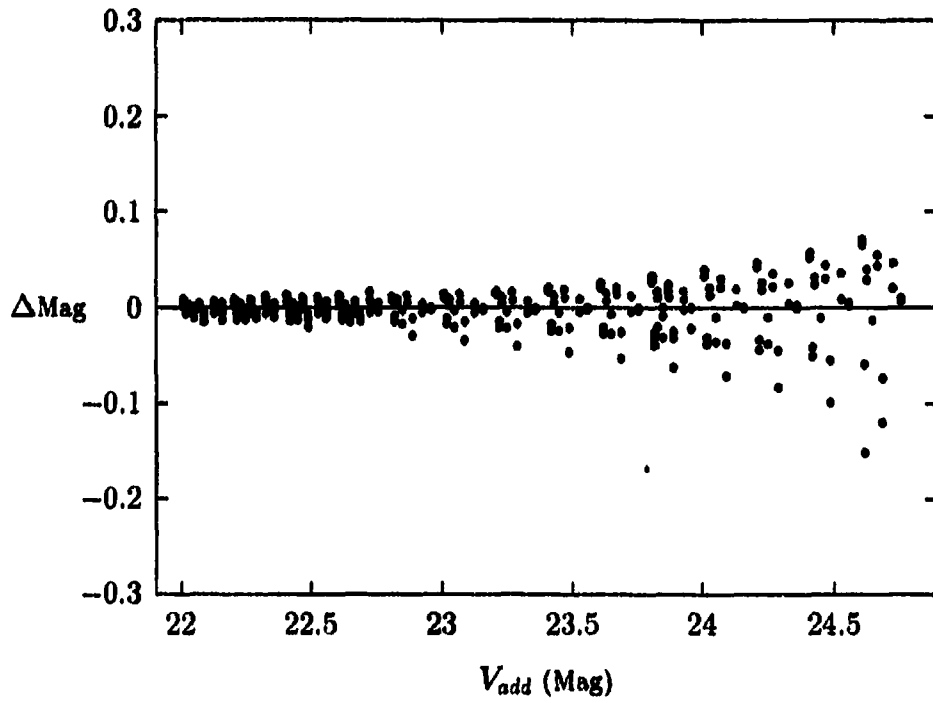


Figure 3.12: Plot of the magnitude difference between added artificial stars (using **Addstar**) and recovered stars, versus V magnitude for added stars in the median filtered HCG 90c field. The scatter about the $\Delta Mag = 0$ axis is defined as the systematic error, which was determined to be negligible for this field.

Over the magnitude range of $V=22.0-24.6$, $\sigma_{v,rms} \simeq 0.04$ for HCG 22a and $\sigma_{v,rms} \simeq 0.03$ for HCG 90c.

Chapter 4

Results

4.1 Globular Cluster Luminosity Function

The globular cluster luminosity function (GCLF) for each galaxy must be constructed from the statistical subtraction of star-like objects from the control field. The star-like objects in the control field will consist of a) true globular clusters, b) foreground stars and c) faint background galaxies which have stellar-like profiles and were misclassified by FOCAS. In fact, most contamination will be due to faint galaxies since one expects less than one foreground star per square arcminute in the magnitude range $V=21-25$ (e.g., Ratnatunga & Bahcall 1985). Since object detection and classification were carried out identically for both control and galaxy fields, the difference in the number of star-like objects between the galaxy fields and the control field (corrected for completeness and normalized with respect to area) should be, statistically, globular cluster candidates.

Before a comparison can be made between objects found in the control field and those found in the galaxy fields, the data must be completeness-corrected. All star-like objects found on the control field were first placed into 0.2 magnitude bins. The completeness data (Table 3.3) were used to correct the total number of objects (per bin) by dividing the raw counts by the completeness fraction for that bin. Thus the corrected counts give an estimate of the total number of objects that would have been detected if the detection process would have been 100% efficient. The number of detected objects also depends upon the size of the field. The total useable area of

the control field (ie. excluding masked out regions due to bad columns, charge traps, etc.) was 47.9 arcmin². The number of corrected objects (per magnitude bin) is given in Table 4.1. The total number of objects found in the control field (completeness corrected), summed over all magnitude bins, was 199.4 ± 13.1 . The uncertainty in the corrected counts is given by (Bolte 1989)

$$\sigma_n^2 \approx \left[\frac{n_{obs}}{f^2} + \frac{(1-f)n_{obs}^2}{n_{added}f^3} \right], \quad (4.1)$$

where

f = completeness fraction (per mag bin),

n_{obs} = raw counts,

n_{added} = the number of artificial stars added (per mag bin).

4.1.1 HCG 22a

For the HCG 22a field, all program objects were placed in 0.2 magnitude bins and completeness corrected following the same procedure used for the control field. The total area of the galaxy field was calculated for radii between 70 and 441 pixels from the centre of HCG 22a (excluding all masked out regions). The total useable area was determined to be 13.2 arcmins². In order to normalize the control field counts to the galaxy area, the background completeness-corrected counts (per bin) were multiplied by a factor of ~ 0.3 .

The number of globular cluster candidates per magnitude bin was then calculated by subtracting the control field counts (corrected for completeness and area) from the galaxy counts (corrected). Table 4.1 gives the data for HCG 22a and the control field, where N_{gal} is the (completeness corrected) counts for HCG 22a, N_{bgd} is the completeness corrected (and normalized for area) counts for the control field and N is (statistically) the number of globular clusters candidates.

Globular cluster luminosity functions are universally well fitted by either a Gaussian (Harris 1991) or a t_8 function (Secker 1992). The Gaussian function is of the

Table 4.1: Globular Cluster Luminosity Function Data: HCG 22a.

V	$N_{gal.}$	N_{bkgd}	N
22.0-22.2	3.0 ± 1.7	0.6 ± 0.4	2.4 ± 1.8
22.2-22.4	3.0 ± 1.7	2.2 ± 0.8	0.8 ± 1.9
22.4-22.6	0	0.8 ± 0.5	-0.8 ± 0.5
22.6-22.8	5.0 ± 2.2	1.4 ± 0.6	3.6 ± 2.3
22.8-23.0	7.0 ± 2.6	2.8 ± 0.9	4.2 ± 2.8
23.0-23.2	3.1 ± 1.8	0.6 ± 0.4	2.5 ± 1.8
23.2-23.4	9.3 ± 3.1	1.6 ± 0.3	7.6 ± 3.1
23.4-23.6	8.1 ± 2.9	2.8 ± 0.9	5.4 ± 3.0
23.6-23.8	14.2 ± 4.2	4.4 ± 1.1	9.7 ± 4.3
23.8-24.0	16.1 ± 4.4	7.2 ± 1.4	9.0 ± 4.6
24.0-24.2	10.6 ± 3.4	10.0 ± 1.6	0.6 ± 3.8
24.2-24.4	35.4 ± 6.6	8.8 ± 1.7	26.6 ± 6.8
24.4-24.6	30.2 ± 7.0	12.0 ± 2.0	18.2 ± 7.3

form

$$N(V) = A \exp \left[-\frac{(m - m_o)^2}{2\sigma^2} \right], \quad (4.2)$$

where

$N(V)$ = number of globular clusters,

A = Gaussian function scale factor,

m = V magnitude of globular clusters,

m_o = V magnitude of the Gaussian function peak,

σ = dispersion of the Gaussian function.

The fit of the Gaussian function to the GCLF data involves the simultaneous fitting of three parameters (turnover, dispersion and scale factor). Since the GCLF data for HCG 22a are highly uncertain, especially near the magnitude limit of the data, it was decided not to perform a direct fit to the GCLF data. In order to determine the turnover in the GCLF, a value for the Hubble parameter was assumed and the distance to HCG 22a was calculated from the median redshift of the group. A redshift value of $z=0.009$ was taken from Hickson et al. (1992) and, assuming $H_o=75$ km/s/Mpc, a distance of 36 Mpc was calculated for HCG 22a. As stated in

the Introduction, the absolute magnitude of the turnover in the GCLF is observed to be roughly the same for all galaxies, regardless of their morphological type or local environment (Harris 1991; Jacoby et al. 1992). We have therefore adopted $M_v = -7.4 \pm 0.2$ for the absolute magnitude of the turnover, which is consistent with previous studies (e.g., Fleming et al. 1995). The apparent magnitude of the turnover was then calculated using

$$m_o - M_v = 5 \cdot \log d - 5, \quad (4.3)$$

where

m_o = apparent magnitude,

M_v = absolute magnitude,

d = distance (pc).

The apparent magnitude of the turnover in the GCLF for HCG 22a was determined to be $m_v = 25.4 \pm 0.2$. Figure 4.1 shows a plot of the GCLF for HCG 22a with a Gaussian function having a turnover of $m_v = 25.4 \pm 0.2$, a dispersion of $\sigma = 1.4^1$, and a scale factor of $A=8.76$ (derived from a non-linear least-squares fit to the GCLF using the above stated values for m_v and σ). The above procedure was repeated for $H_o = 50$ km/s/Mpc and a turnover magnitude of $m_o = 26.3 \pm 0.2$ was calculated. Figure 4.1 shows a plot of the Gaussian function using $H_o = 50$ km/s/Mpc.

4.1.2 HCG 90c

The GCLF for HCG 90c was derived in the same manner as that done for HCG 22a. The list of star-like objects consists of those having radii between 60 and 535 pixels from the galaxy centre. A large fraction of the galaxy field was masked out in order to prevent the inclusion of any objects associated with the neighbouring galaxies HCG 90b and d. The inner $R = 60$ pixels of the centre of HCG 90c was masked out as described earlier. The total usable area of the galaxy field was calculated to be 14.9

¹The dispersion of the Gaussian function has been shown to have only a narrow range of values (Harris 1991), centred on $\sigma_{\text{Gauss}} = 1.4$ (Jacoby et al. 1992).

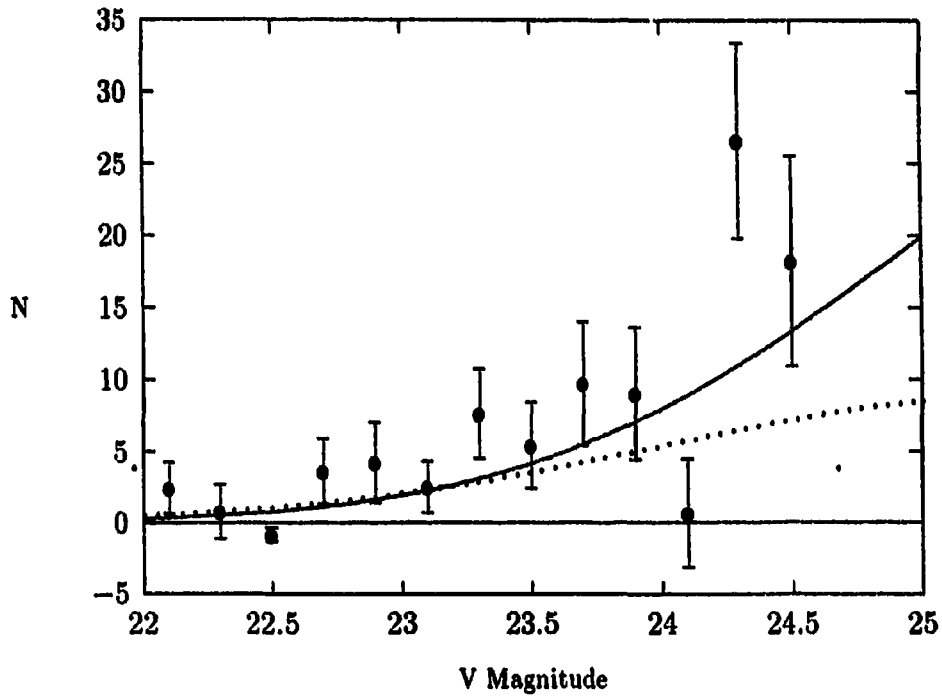


Figure 4.1: Globular cluster luminosity function for HCG 22a. The fit of a Gaussian function (assuming $H_0 = 50$ km/s/Mpc and $\sigma=1.4$) is shown as the solid line with a turnover of $m_V = 26.3 \pm 0.2$. The dotted line is a Gaussian function with a turnover of $m_V = 25.4 \pm 0.2$ (assuming $H_0 = 75$ km/s/Mpc).

arcmin², which is only 31% of the size of the control field. The star-like objects were placed into 0.2 magnitude bins, corrected for completeness and background subtracted (control field counts were completeness corrected and normalized with respect to the area of HCG 90c). The data for HCG 90c is given in Table 4.2.

The turnover in the GCLF for HCG 90c was calculated in the same manner as that for HCG 22a. A median group redshift of $z=0.0088$ was used to derive a distance to HCG 90c by assuming $H_0 = 75$ km/s/Mpc. Using the same absolute magnitude for the turnover as applied to HCG 22a, the apparent magnitude of the GCLF was determined to be $m_V = 25.1 \pm 0.2$. The above calculations were repeated using $H_0 = 50$ km/s/Mpc and the turnover apparent magnitude was found to be $m_V = 26.0 \pm 0.2$. Table 4.3 summarizes the values of the turnover in the GCLF for HCG 22a and HCG 90c using two different values for the Hubble parameter. Figure 4.2 shows the GCLF for HCG 90c along with the calculated Gaussian function for $H_0 = 50$ and 75

Table 4.2: Globular Cluster Luminosity Function Data: HCG 90c.

V	$N_{gal.}$	N_{bkgd}	N
22.0-22.2	6.0 ± 2.4	0.6 ± 0.4	5.4 ± 2.5
22.2-22.4	6.0 ± 2.4	2.5 ± 0.9	3.5 ± 2.6
22.4-22.6	8.0 ± 2.8	0.9 ± 0.5	7.1 ± 2.9
22.6-22.8	6.0 ± 2.4	1.6 ± 0.4	4.4 ± 2.5
22.8-23.0	13.0 ± 3.6	3.1 ± 1.0	9.9 ± 3.7
23.0-23.2	15.0 ± 3.9	0.6 ± 0.4	14.4 ± 3.9
23.2-23.4	6.0 ± 2.4	1.9 ± 0.8	4.1 ± 2.6
23.4-23.6	10.0 ± 3.2	3.1 ± 1.0	6.9 ± 3.3
23.6-23.8	20.0 ± 4.5	5.0 ± 1.2	15.0 ± 4.6
23.8-24.0	22.0 ± 4.7	8.1 ± 1.6	13.9 ± 5.0
24.0-24.2	26.0 ± 5.1	11.2 ± 1.9	14.8 ± 5.4
24.2-24.4	50.1 ± 7.4	9.9 ± 1.9	40.2 ± 7.7
24.4-24.6	38.8 ± 6.9	13.5 ± 2.3	25.4 ± 7.2

Table 4.3: GCLF turnover apparent magnitudes.

Galaxy	H_0 (km/s/Mpc)	m_V
HCG 22a	50	26.3 ± 0.2
	75	25.4 ± 0.2
HCG 90c	50	26.0 ± 0.2
	75	25.1 ± 0.2

km/s/Mpc.

4.2 Radial Distribution: HCG 22a

The radial distribution of the globular cluster population was determined for each galaxy by dividing the fields into several annuli. For HCG 22a, the globular cluster population was divided into seven annuli (53 pixels in width) between a radius of 70 and 441 pixels. For each annulus, the total number of globular cluster candidates was corrected for completeness (over the magnitude range used previously) and the surface density of objects (per arcmin²) was then computed. Next, the density of star-like objects in the control field was calculated (completeness corrected) and this

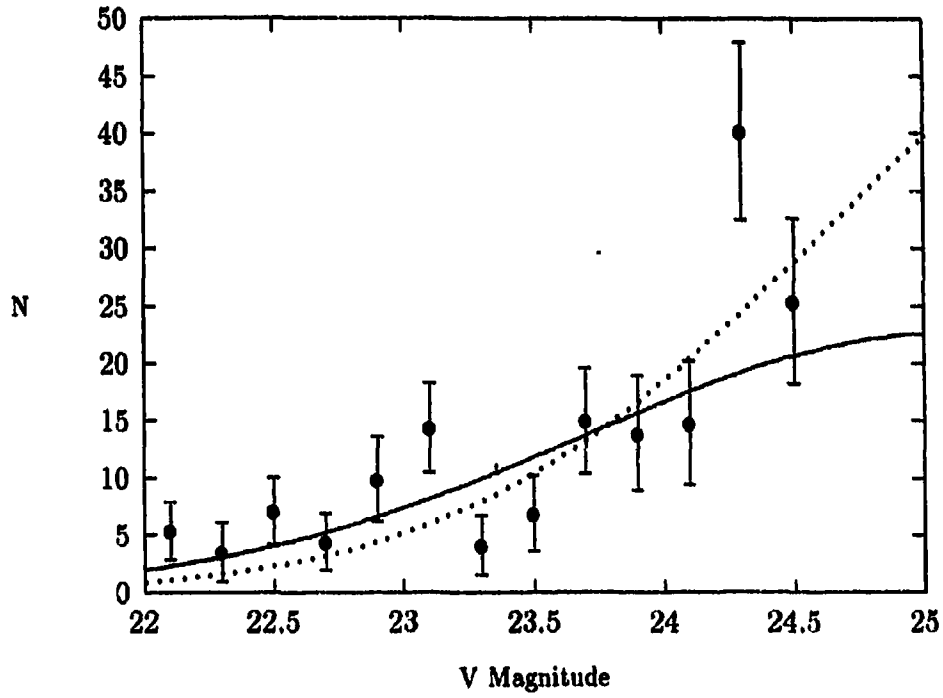


Figure 4.2: Globular cluster luminosity function for HCG 90c. The fit of a Gaussian function (assuming $H_o = 50$ km/s/Mpc and $\sigma=1.4$) is shown as the solid line with a turnover of $m_V = 26.0 \pm 0.2$. The dotted line is a Gaussian function with a turnover of $m_V = 25.1 \pm 0.2$ (assuming $H_o = 75$ km/s/Mpc).

value ($\sigma_{bgd} = 4.2$ clusters/arcmin²) was subtracted from the density determined for each of the annuli in the galaxy field. This final value should be, statistically, the density of globular clusters. Table 4.4 gives the values determined for HCG 22a. The second column of the table lists the density of globular clusters (completeness corrected and background subtracted). All uncertainties are added in quadrature and follow the work of Bolte (1989).

In order to characterize the radial distribution of globular clusters, a power-law of the form, $\sigma = AR^\alpha$, was fitted to the data (e.g., Fleming et al. 1995). Using weighted nonlinear least-squares, the best-fit values for the radial distribution for HCG 22a was found to be

$$A = 7.21 \pm 1.28,$$

$$\alpha = -2.01 \pm 0.30,$$

with $\chi^2 = 6.4$ and a reduced $\chi^2 = 1.3$. Figure 4.3 shows the radial distribution of the

Table 4.4: Globular Cluster Radial Distribution Data: HCG 22a.

R (arcmin)	σ_{cl} (clusters/arcmin ²)
0.34-0.59	33.1 ± 7.9
0.59-0.85	19.5 ± 5.0
0.85-1.10	5.7 ± 2.8
1.10-1.36	8.1 ± 2.8
1.36-1.62	4.1 ± 2.0
1.62-1.87	0.3 ± 1.3
1.87-2.13	3.3 ± 1.8

globular cluster population for HCG 22a, along with the best-fit power-law.

A useful comparison can also be made between the spatial extent of the globular cluster system and the stellar halo of the parent galaxy. Figure 4.4 shows a comparison of the radial profile of the globular cluster system and the surface brightness for HCG 22a (R magnitude). The surface brightness data has been taken from Franx et al. (1989) and has been scaled vertically to match the GC profile near its centre. A fit to the halo profile gives, $\mu \sim R^{-2.3}$, which is equal to the slope of the radial profile of the GCs ($\alpha = -2.01 \pm 0.3$). Thus the globular cluster system is as spatially extended as the halo light of HCG 22a. This is consistent with other studies where the GC profiles are either similar to or more extended than the galaxy halo (e.g., Fleming et al. 1995).

The radial distribution of HCG 22a can also be compared to the relationship between the total absolute V magnitude of the galaxy and the exponent of the power-law fit to the GC radial profile. This relation is given as (see Harris 1993)

$$\alpha = (-0.29 \pm 0.03)M_v^T - 4.49, \quad (4.4)$$

where α is defined as $\sigma \sim R^{-\alpha}$ and the observed scatter in α is ± 0.2 . The absolute magnitude of HCG 22a was determined by calculating the distance to the galaxy using the equation

$$D = v/H_o, \quad (4.5)$$

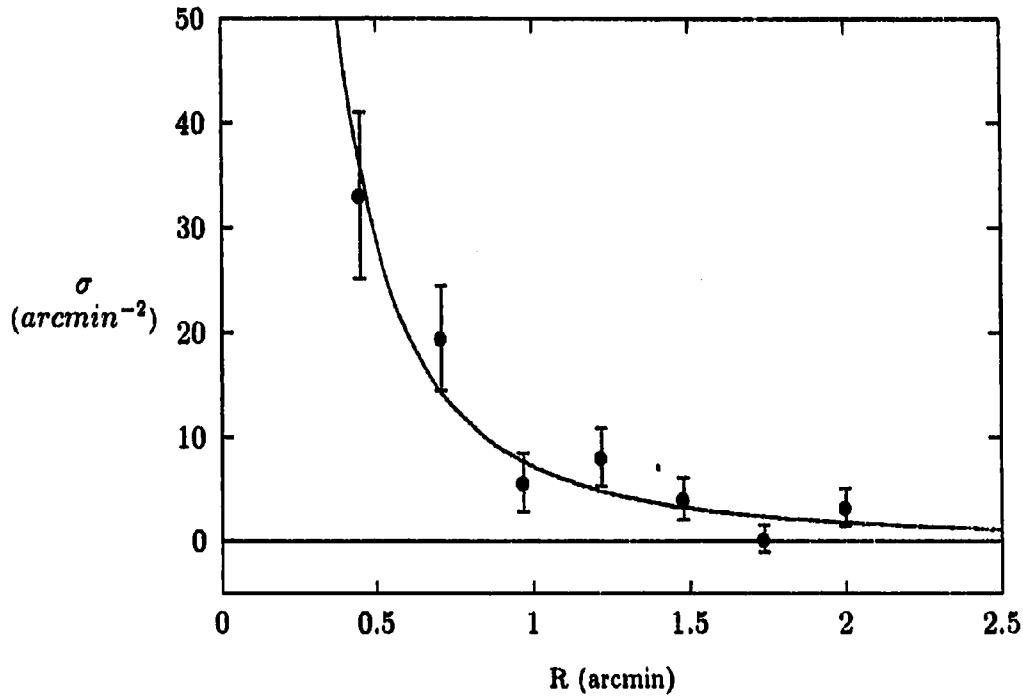


Figure 4.3: Radial distribution of globular clusters around HCG 22a. σ is the number of star-like objects per arcmin² (completeness corrected and background subtracted). The radius is given as the geometric mean of the annuli ($\langle R \rangle = \sqrt{R_{inner} R_{outer}}$) in arcminutes. The best-fit power-law function is shown as the solid line.

where

D = distance,

v = median radial velocity of the group,

H_o = the Hubble parameter,

and using equation 4.3 (along with a value for the apparent magnitude) to calculate the absolute magnitude. The apparent magnitude for HCG 22a was obtained from the RC3 catalog (1991) using the NED² and was listed as $m_V^r = 11.35 \pm 0.07$. For $H_o = 50$ km/s/Mpc, $M_V = -22.31 \pm 0.07$ and for $H_o = 75$ km/s/Mpc, $M_V = -21.43 \pm 0.07$. Using equation 4.4, the predicted values of α equals -1.98 ± 0.02 and -1.72 ± 0.02 (for $H_o = 50$ and 75 km/s/Mpc). These values are consistent with the value obtained by fitting a power-law to the radial distribution ($\alpha_{HCG22a} = -2.01 \pm 0.3$).

²The NASA/IPAC extragalactic database (NED) is operated by the Jet Propulsion Laboratory, California Institute of Technology, under contract with the National Aeronautics and Space Administration.

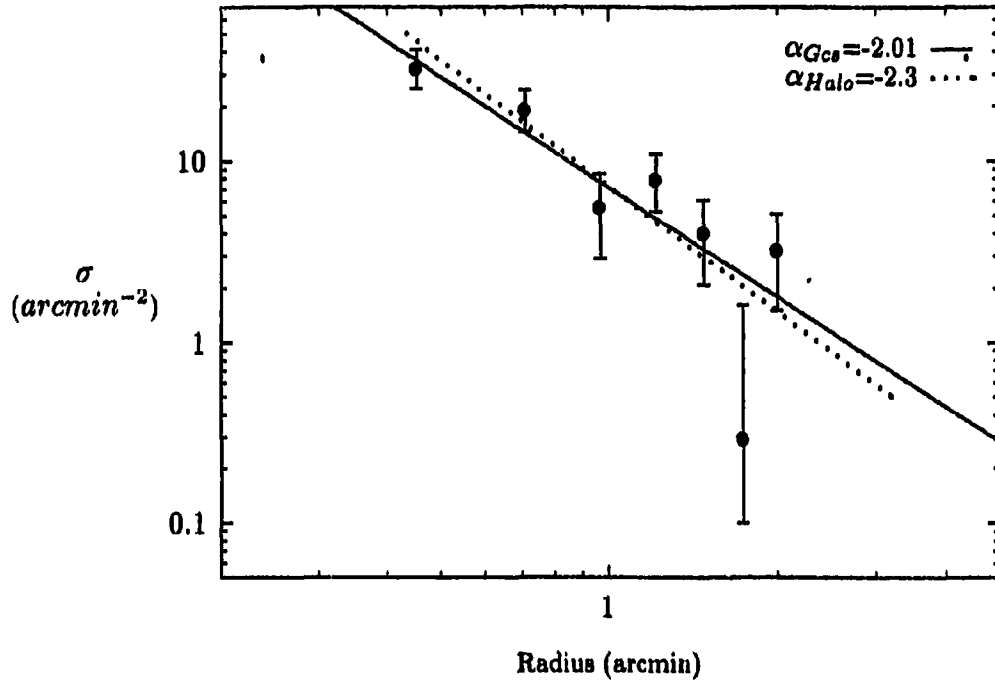


Figure 4.4: The radial profile of the globular cluster system of HCG 22a (solid dots with error bars), compared to the surface brightness (R magnitude) from Franx et al. (1989). The surface brightness profile has been arbitrary scaled in height in order to match the GC profile near it's centre. From the figure, it is clear that the globular cluster system is as spatially extended as the halo light of the parent galaxy. The slope of a power-law fit to the GC profile is $\alpha = -2.01 \pm 0.3$ while for the halo light, the slope is $\alpha = -2.3$.

Table 4.5: Globular Cluster Radial Distribution Data: HCG 90c.

R (arcmin)	σ_{cl} (clusters/arcmin ²)
0.29-0.41	46.9 ± 16.2
0.41-0.53	30.7 ± 11.6
0.53-0.65	14.1 ± 7.5
0.65-0.77	25.1 ± 8.8
0.77-0.89	18.6 ± 7.2
0.89-1.01	23.8 ± 7.5
1.01-1.13	27.3 ± 7.4
1.13-1.25	14.2 ± 5.3
1.25-1.37	26.4 ± 6.5
1.37-1.50	10.0 ± 4.3
1.50-1.62	9.1 ± 4.0
1.62-1.74	7.9 ± 3.6
1.74-1.86	11.2 ± 4.0
1.86-1.98	9.4 ± 3.6
1.98-2.10	10.2 ± 3.6
2.10-2.22	2.1 ± 2.4
2.22-2.34	2.1 ± 2.4
2.34-2.46	2.7 ± 2.5
2.46-2.58	1.5 ± 2.1

4.3 Radial Distribution: HCG 90c

For HCG 90c, the radial distribution was calculated in bins from 60 to 535 pixels in radius (with the exclusion of the masked out regions as mentioned previously). The radial profile was determined by dividing the area around HCG 90c into 19 annuli of width 25 pixels. The procedure in calculating the density of globular clusters for each annulus was similar to that used for HCG 22a. The raw counts were completeness corrected and the background density was subtracted. The data for the radial distribution of HCG 90c is given in Table 4.5.

A power-law fit to the radial data gives best-fit values of $\alpha = -1.20 \pm 0.16$ and $A = 13.99 \pm 1.42$ with a $\chi^2_\nu = 1.5$. This analysis was made using a weighted non-linear least-squares fit to the data. Figure 4.5 shows the radial profile, along with the best fit power-law, for HCG 90c.

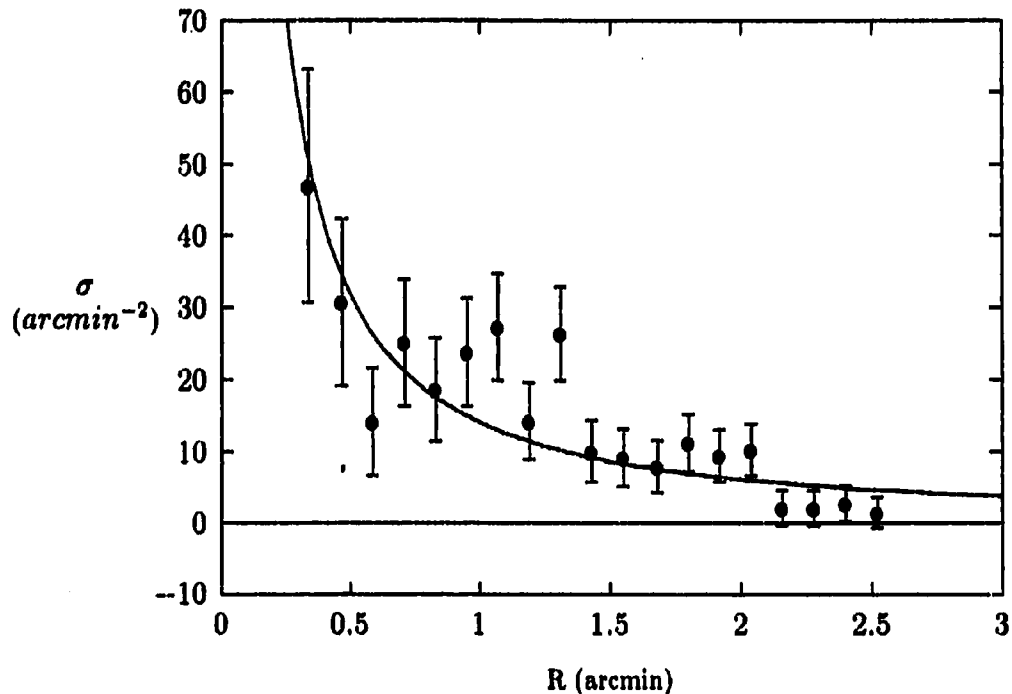


Figure 4.5: Radial distribution of globular clusters around HCG 90c. σ is the number of star-like objects per arcmin² (completeness corrected and background subtracted). The best-fit power-law function is shown as the solid line.

The value for α was calculated using the relationship between M_v and α (equation 4.4) following the procedure used for HCG 22a. The apparent magnitude of HCG 90c was listed as $m_V^T = 11.62$ in the RC3 (1991) catalog (no uncertainty given). Using the median redshift of HCG 90 ($z=0.0088$; Hickson et al. 1992), the absolute magnitude of HCG 90c was determined to be $M_V = -21.79$ (for $H_o = 50$ km/s/Mpc) and $M_V = -20.91$ (for $H_o = 75$ km/s/Mpc). Equation 4.4 gives values for α of 1.83 ± 0.2 and 1.57 ± 0.2 (for $H_o = 50$ and 75 km/s/Mpc). These values do not agree with the fitted value of $\alpha_{HCG90c} = -1.20 \pm 0.16$. The shallower slope for HCG 90c may be the result of contamination from the globular clusters of other galaxies in the HCG 90 group.

4.4 Specific Frequency: HCG 22a

As discussed in the Introduction, a useful way of quantifying the globular cluster populations of different galaxies is to compare values of specific frequency. The specific

frequency is defined as the number of globular cluster per unit galaxy luminosity (normalized to $M_v = -15$; van den Bergh & Harris 1982) and is given by

$$S_N = N_{total} 10^{0.4(M_v^T + 15)}, \quad (4.6)$$

where

S_N = specific frequency,

N_{total} = the total number of globular clusters,

M_v^T = the absolute V magnitude of the parent galaxy.

The first step in calculating the specific frequency is to determine N_{total} . The power-law function, $\sigma = AR^\alpha$, must be integrated from an inner radius to an outer radius in order to account for the globular clusters that were missed due to spatial incompleteness. Also, the number of globular clusters must be corrected for the incomplete coverage of the luminosity function.

In order to integrate over the radial globular cluster distribution, inner and outer radius limits must be adopted. Globular cluster distributions normally do not extend to radii inward of 1 kpc from the centre of the parent galaxy (e.g. Harris 1991; Bridges, Hanes, & Harris 1991). The most likely cause is that tidal shocking and dynamical friction will destroy globular clusters at distances close to the galaxy centre (e.g. Weinberg 1993). For an outer radius, globular cluster systems generally do not extend past 50 kpc from the centre of a typical elliptical galaxy (e.g. Harris & van den Bergh 1981; Hanes & Harris 1986; Fleming et al. 1995). Thus for this study, an inner radius of 1 kpc and an outer radius of 50 kpc was used which correspond to angular distances of 0.06' and 3.18' (for $H_o = 50$ km/s/Mpc) and 0.10' and 4.75' (for $H_o = 75$ km/s/Mpc), respectively (it is important to note that the radial counts for HCG 22a and HCG 90c appear to reach background levels ~ 50 kpc from the galaxy centre).

The integral of the power-law density profile gives

$$N_{total} = \int \sigma_{cl} da, \quad (4.7)$$

where

$$da = 2\pi R dR. \quad (4.8)$$

Thus, we have (using $H_o = 50$ km/s/Mpc)

$$N_{total} = 2\pi A \int_{0.06'}^{3.18'} R^{\alpha+1} dR. \quad (4.9)$$

Solving equation 4.9, the total number of globular clusters belonging to HCG 22a is

$$N_{total} = 181 \pm 56,$$

(note that this does not yet include correction for faint globular clusters below our detection limit). If the outer radius was set at a smaller value, say 25 kpc, the total number of globular clusters would be (~ 148) and hence N_{total} is not too sensitive for a steep slope like $\alpha \sim -2.0$. The uncertainty in N_{total} , was determined using the standard error equation

$$\sigma_{N_{tot}}^2 = \sigma_A^2 \left(\frac{\partial N_{tot}}{\partial A} \right)^2 + \sigma_\alpha^2 \left(\frac{\partial N_{tot}}{\partial \alpha} \right)^2. \quad (4.10)$$

After correcting for the radial incompleteness of detected globular clusters, the incomplete coverage of the luminosity function must be accounted for. Since the luminosity function was assumed to be Gaussian in shape, the area under the part of the Gaussian unaccounted for in the data will give a measure of the percent of unobserved globular clusters. Integrating the Gaussian curve from $-\infty$ to the photometric limit of the data ($V = 24.6$), the total observed part of the Gaussian distribution equals $11 \pm 6\%$ of the total. Correcting N_{total} for the unobserved part of the luminosity function, the total number of globular clusters (corrected) is

$$N_{total}^{corrected} = 1645 \pm 608.$$

Once the total number of globular clusters have been calculated, the absolute V magnitude of the parent galaxy ($M_V = -22.31 \pm 0.07$ for $H_o = 50$ km/s/Mpc) can

be used to determine S_N . From Equation 4.6, the computed specific frequency for HCG 22a is

$$S_N = 2.0 \pm 0.7.$$

The uncertainty in S_N , was determined using the standard error equation

$$\sigma_{S_N}^2 = \sigma_{N_{tot}}^2 \left(\frac{\partial S_N}{\partial N_{tot}} \right)^2 + \sigma_{M_v^{tot}}^2 \left(\frac{\partial S_N}{\partial M_v^{tot}} \right)^2. \quad (4.11)$$

Repeating the above calculations for S_N using $H_o = 75$ km/s/Mpc, the specific frequency is

$$S_N = 1.7 \pm 0.8.$$

4.5 Specific Frequency: HCG 90c

The specific frequency of HCG 90c was calculated using the same procedure as that used for HCG 22a. For $H_o = 50$ km/s/Mpc (and a median group redshift $z=0.0088$), the limits of integration for the radial distribution were determined to be

$$R_{in} = 1 \text{ kpc} = 0.07',$$

$$R_{out} = 50 \text{ kpc} = 3.5'.$$

The total number of globular clusters over this range of radius is . . .

$$N_{total} = 2\pi A \int_{0.07'}^{3.5'} R^{\alpha+1} dR. \quad (4.12)$$

For our observed value $\alpha = -1.20$, this yields

$$N_{tot} = 286 \pm 30,$$

where the uncertainty in N_{tot} was again calculated from Equation 4.10. If an outer radius of 25 kpc is used, $N_{total} \sim 159$ and thus the total number of globular clusters is sensitive on the choice of an outer radius for a slope of $\alpha \sim -1.2$.

Table 4.6: Summary of specific frequency values.

Galaxy	H_0 (km/s/Mpc)	S_N
HCG 22a	50	2.0 ± 0.7
	75	1.7 ± 0.8
HCG 90c	50	3.4 ± 1.2
	75	4.8 ± 1.0

Correcting for the unobserved part of the luminosity function (again integrating a Gaussian function from $-\infty$ to the photometric limit of $m_v = 24.6$), we determined that $16 \pm 4\%$ of the total number of globular clusters have been observed. Correcting N_{total} for the unobserved portion of the luminosity function, we have

$$N_{total}^{corrected} = 1788 \pm 635.$$

Using the value of absolute magnitude as calculated above for $H_0 = 50$ km/s/Mpc, the specific frequency for HCG 90c is

$$S_N = 3.4 \pm 1.2,$$

where the uncertainty was calculated as before.

Repeating the above calculations for S_N using $H_0 = 75$ km/s/Mpc, the specific frequency is

$$S_N = 4.8 \pm 1.0.$$

Table 4.6 summarizes the calculated values of specific frequency with different values of H_0 .

Chapter 5

Discussion

Although our sample is limited to only two compact group galaxies, we can draw some tentative conclusions. The most important aspect of this study is the determination of the specific frequencies of HCG 22a and HCG 90c. As mentioned in the Introduction, specific frequency values generally range from 2–3 for field ellipticals and 5–7 for ellipticals in rich galaxy clusters. The relatively low S_N values determined for both HCG 22a and HCG 90c ($S_N \sim 2.0$ and $S_N \sim 4$) are consistent with the hypothesis that these globular cluster systems were formed at a time when their parent galaxy was simply a ‘field’ elliptical or in a low density environment.

If HCG 22a and HCG 90c were formed in a high density environment, like that found in compact groups, one might expect higher specific frequency values if the formation of globular clusters was more efficient in higher density environments (e.g., ‘biased’ globular cluster formation; West 1993). As stated in the introduction, specific frequency values seem to follow the general trend that as the local density increases, the number of globular clusters (per unit galaxy luminosity) also increases (Figure 1.1). It is also interesting to note that all high S_N galaxies are found in high density environments (e.g., M87 and NGC 1399; Harris 1991), such as the centres of rich Abell clusters, but that not all galaxies sitting at the centre of these rich clusters are high S_N systems (Harris, Pritchet & McClure 1995). Thus the evidence seems to suggest that a high density environment, at least at the current epoch, is a necessary but not a sufficient condition for the formation of high S_N galaxies.

Besides providing possible insights into globular cluster formation, the results of this study may be pointing the way to the true nature of compact groups. The exact nature of Hickson compact groups has been controversial since some studies have suggested that Hickson compact groups are really only chance projections of large filamentary structures (Hernquist, Katz & Weinberg 1995) or superposition of galaxies in a much larger group or poor cluster (e.g., Walke & Mamon 1989). The basic reason given for this suggestion is that N-body simulations hint at the possibility that (given the small crossing times and low velocity dispersions of compact group members; Hickson et al. 1992) member galaxies should merge to form a single elliptical on the order of a few crossing times (e.g., Barnes 1985; Mamon 1987). This would indicate that compact group members are just beginning to come together at the present time and that in the past the current member galaxies were in a lower local density environment. The small values of S_N found for HCG 22a and HCG 90c are consistent with this idea since the specific frequency values are characteristic of galaxies found in low density environments (Harris 1991).

There is a lot of evidence that seems to suggest that most Hickson compact groups are truly compact (Mendes de Oliveira & Hickson 1994). The detection of H_I (Williams & Rood 1987) and of X-rays (e.g., Pildis, Bregman & Evrard 1995) surrounding some Hickson compact groups suggest that these galaxies have undergone significant dynamical evolution and that galaxy interactions may have occurred (Mendes de Oliveira & Hickson 1994). Other evidence for true 'compactness' is that the fraction of spiral galaxies per group decreases with decreasing crossing times (Hickson et al. 1992). The common interpretation of this fact is that groups with smaller crossing times have had time for member spiral galaxies to merge and form elliptical galaxies. This can only be possible if these compact groups are physically nearby to each other (Hickson et al. 1992). Further evidence that supports the idea that most compact groups are truly compact is the presence of tidal tails and tidal debris in some compact groups. Hunsberger, Charlton & Zaritsky (1996) report the

discovery of 47 dwarf galaxy candidates in the tidal features of a sample of 42 Hickson compact groups (HCG 22 and HCG 90c were not part of the study). This provides strong evidence to support the idea that most of the Hickson compact groups are real physical associations.

The results from this study are unable to prove whether or not HCG 22a and HCG 90c were located in a dense 'compact-like' environment at the time when their globular cluster systems were formed. For HCG 22 and HCG 90, both compact groups have been detected in X-rays with HCG 90 being more X-ray luminous than HCG 22 (Ponman et al. 1996). As stated previously, HCG 90 also contains a galaxy (HCG 90d) which is clearly interacting with another galaxy (Hickson 1994). Thus the above evidence suggest that the target groups in this study are truly compact groups. It is of interest to note that the radial profile of HCG 90c ($\alpha = -1.20 \pm 0.16$) is a lot shallower than the radial profile of HCG 22a ($\alpha = -2.01 \pm 0.3$). With the large uncertainties involved in the study of the radial distribution of these galaxies it is unclear how concrete these results are.

From the results of this study, it is clear that further observations are needed to help understand both the formation of globular clusters and the nature of Hickson compact groups. Observations which clearly reach the turnover would be of great value since they would provide a direct determination of the distance to member galaxies. Also, a high signal-to-noise ratio in the number of detected GCs would decrease the uncertainties associated with the GCLF and radial distribution. Also needed are observations of a larger sample of compact group galaxies. This would help to provide possible evidence for any correlation between galaxy luminosity and S_N (since the local environment would be the same for a pair of galaxies in the same group) or other factors such as X-ray luminosity, mass-to-light ratio and distance from the group dynamical centre.

Chapter 6

Summary and Conclusion

We have measured the globular cluster populations of galaxies in Hickson compact groups for the first time. Deep V and R CCD images of HCG 22a and HCG 90c were obtained on October 9–10, 1993 using the European Southern Observatory's New Technology Telescope. The globular cluster populations have been measured by removing the parent galaxy light and detecting and classifying objects using FOCAS. The GCLF of each galaxy has been measured and an estimate of their distance has been calculated by assuming an absolute magnitude for the GCLF turnover and solving for the apparent magnitude using the group median redshift and an assumed value for the Hubble parameter. The radial profile of each galaxy was measured and the value for the slopes (using a powerlaw of $\sigma = AR^\alpha$) was determined to be $\alpha = -2.01 \pm 0.30$ for HCG 22a and $\alpha = -1.20 \pm 0.16$ for HCG 90c. Using a value of $H_0 = 50$ km/s/Mpc, the specific frequency for HCG 22a is $S_N = 2.0 \pm 0.7$ and $S_N = 3.4 \pm 1.2$ for HCG 90c. Using a value of $H_0 = 75$ km/s/Mpc, $S_N = 1.7 \pm 0.8$ for HCG 22a and $S_N = 4.8 \pm 1.0$ for HCG 90c. The derived specific frequency values of for HCG 22a and HCG 90c are similar to the values found for field elliptical galaxies (Harris 1991).

Chapter 7

References

- Ashman, K. M., & Zepf, S. E. 1992, *ApJ*, 384, 50
- Barnes, J. 1985, *MNRAS*, 215, 517
- Bolte, M. 1989, *ApJ*, 341, 168
- Bridges, T. J., Hanes, D. A., & Harris, W. E. 1991, *AJ*, 101, 469
- Butterworth, S. T., & Harris, W. E. 1992, *AJ*, 103, 1828
- Chaboyer, B., Demarque, P., & Sarajedini, A. 1996, *ApJ*, 459, 558
- Chaboyer, B., Kernan, P. J., Krauss, L. M., & Demarque, P. 1996, *Science*, 271, 957
- de Vaucouleurs, G., de Vaucouleurs, A., Corwin, H. G., Buta, R. J., Paturel, G., & Fouqué, P. 1991, *Third Reference Catalogue of Bright Galaxies* (Springer, New York (RC3))
- Ebeling, H., Voges, W., & Böhringer, H. 1994, *ApJ*, 436, 44
- Eggen, O. J., Lynden-Bell, D., & Sandage, A. R. 1962, *ApJ*, 136, 748
- Fabian, A. C., Nulsen, P. E. J., & Canizares, C. R. 1984, *Nature*, 310, 733
- Fall, S. M., & Rees, M. J. 1985, *ApJ*, 298, 18
- Fischer, P., Hesser, J. E., Harris, H. C., & Bothun, G. D. 1990, *PASP*, 102, 5
- Fleming, D. E. B., Harris, W. E., Pritchett, C. J., & Hanes, D. A. 1995, *AJ*, 109, 1044
- Franx, M., Illingworth, G., & Heckman, T. 1989, *AJ*, 98, 538
- Hanes, D. A., & Harris, W. E. 1986, *ApJ*, 309, 564
- Harris, W. E. 1987, *ApJ*, 315, L29
- . 1989, in *Modern Instrumentation and Techniques*, McMaster Graduate Work-

shop

—. 1990, *PASP*, 102, 949

—. 1991, *ARA&A*, 29, 543

—. 1993, in *ASP Conf. Ser. 48, The Globular Cluster-Galaxy Connection*, ed. G. Smith & J. Brodie (San Francisco: ASP), 472

—. 1995, private communication

Harris, W. E., Pritchett, C. J., & McClure, R. D. 1995, *ApJ*, 441, 120

Harris, W. E., & Pudritz, R. E. 1994, *ApJ*, 429, 177

Harris, W. E., & van den Bergh, S. 1981, *AJ*, 86, 1627

Hernquist, L., Katz, N. S., & Weinberg, D. H. 1995, *ApJ*, 442, 57

Hickson, P. 1982, *ApJ*, 255, 382

—. 1994, in *Atlas of Compact Groups of Galaxies* (Gordon and Breach Science Publishers)

Hickson, P., Mendes De Oliveira, C., Huchra, J. P., & Palumbo, G. G. C. 1992, *ApJ*, 399, 353

Hintzen, P., Romanishin, W., & Valdis, F. 1991, *ApJ*, 366, 7

Howell, S. B. 1989, *PASP*, 101, 616

Hunsberger, S. D., Charlton, J. C., & Zaritsky, D. 1996, *ApJ*, 462, 50

Jacoby, G. H., Branch, D., Ciardullo, R., Davies, R. L., Harris, W. E., Pierce, M. J., Pritchett, C. J., Tonry, J. L., & Welch, D. L. 1992, *PASP*, 104, 599

Jarvis, J. F., & Tyson, J. F. 1981, *AJ*, 86, 476

Jedrzejewski, R. I. 1987, *MNRAS*, 226, 747

Jimenez, R., Thejll, P., Jørgensen, U. G., MacDonald, J., & Pagel, B. 1996, preprint

Landolt, A. U. 1992, *AJ*, 104, 340

Mamon, G. A. 1987, *ApJ*, 321, 622

Mendes de Oliveira, C., & Hickson, P. 1994, *ApJ*, 427, 684

Neuschaefer, L. W., Ratnatunga, K. U., Griffiths, R. E., Valdes, F. 1995, *PASP*, 107, 590

- Ostriker, J. P., Lubin, L. M., & Hernquist, L. 1995, *ApJ*, 444, L61
- Peterson, C. 1993, in *Structure and Dynamics of Globular Clusters*, ASP Conf. Ser., 50, 337
- Pildis, R. A., Bregman, J. N., & Evrard, A. E. 1995, *ApJ*, 443, 514
- Ponman, T. J., & Bertram, D. 1993, *Nature*, 363, 51
- Ponman, T. J., Bourner, P. D. J., Ebeling, H., & Böhringer, H. 1996, preprint
- Ratnatunga, K. U., & Bahcall, J. N. 1985, *ApJS*, 59, 63
- Rood, H. J., & Williams, B. A. 1989, *ApJ*, 339, 772
- Röttgering, H. J. A., Miley, G. K., Chambers, K. C., & Macchetto, F. 1995, *A&AS*, 114, 51
- Searle, L., & Zinn, R. 1978, *ApJ*, 225, 357
- Secker, J. 1992, *AJ*, 104, 1472
- . 1995, *PASP*, 107, 496
- Stetson, P. B. 1990, *PASP*, 102, 932
- Stetson, P. B., Davis, L. E., & Crabtree, D. R. 1990, in *CCDs in Astronomy*, ASP Conf. Ser. 8, edited by G.H. Jacoby (ASP, San Francisco), p. 289
- Stetson, P. B., Vandenberg, D. A., & Bolte, M. 1996, preprint
- Thompson, L. A., & Valdes, F. 1987, *ApJ*, 315, L35
- Tully, B. 1988, *Nearby Galaxies Catalog* (Cambridge, New York: Cambridge University Press)
- Valdes, F. 1982, *SPIE*, 331, 465
- . 1993, *FOCAS User's Guide*, NOAO document
- Valdes, F., Campusano, L. E., Velásquez, J. D., & Stetson, P. B. 1995, *PASP*, 107, 1119
- Walke, D. G., & Mamon, G. A. 1989, *A & A*, 295, 291
- West, M. J. 1993, *MNRAS*, 265, 755
- West, M. J., Côté, P., Jones, C., Forman, W., & Marzke, O. 1995, *ApJ*, 453, L77
- Williams, B. A., & Rood, H. J. 1987, *ApJS*, 63, 265

Zepf, S. E., & Ashman, K. M. 1993, MNRAS, 264, 611

Zepf, S. E., Ashman, K. M., & Geisler, D. 1995, ApJ, 443, 570

Appendix A

Table A.1: Photometry of globular cluster candidates in HCG 22a. All length units are in pixels with X increasing towards the East and Y towards the North (on the sky). The centre of the galaxy is located at X=885 and Y=647.

ID#	X	Y	V	σ_V	V-R	σ_{V-R}	Radius
1	869.799	575.994	24.357	0.066	0.769	0.091	72.61
2	897.936	574.429	23.635	0.049	0.437	0.063	73.71
3	915.799	580.005	23.924	0.057	0.795	0.072	73.74
4	959.884	653.982	23.600	0.033	0.531	0.056	75.21
5	960.208	661.249	24.404	0.064	0.350	0.137	76.55
6	940.708	589.084	24.336	0.061	0.678	0.098	80.36
7	804.504	639.308	23.612	0.041	0.468	0.075	80.86
8	810.455	614.587	22.938	0.026	0.635	0.036	81.29
9	816.127	690.881	23.830	0.039	0.861	0.056	81.66
10	920.373	553.658	23.427	0.026	0.637	0.040	99.82
11	914.961	550.527	22.969	0.022	0.585	0.036	101.02
12	795.316	693.497	24.571	0.063	0.313	0.150	101.02
13	788.693	686.554	24.408	0.070	0.390	0.114	104.11
14	987.177	672.464	22.062	0.011	0.568	0.022	105.30
15	986.753	614.694	23.849	0.038	0.581	0.057	106.76
16	923.970	747.947	23.540	0.065	0.657	0.084	108.21
17	967.167	575.221	22.805	0.017	0.682	0.038	109.10
18	774.610	666.230	24.202	0.059	0.589	0.085	112.05
19	773.105	626.727	23.713	0.031	0.518	0.051	113.72
20	934.528	543.283	23.373	0.049	0.710	0.071	114.94
21	858.787	531.927	24.415	0.072	0.667	0.094	118.02
22	1004.290	632.472	24.533	0.082	0.296	0.124	120.17
23	935.289	536.720	24.341	0.063	0.793	0.076	121.20
24	784.767	731.346	24.244	0.107	0.804	0.136	131.00
25	981.841	558.503	24.242	0.049	0.641	0.072	131.19

Table A.2: HCG 22a photometry—Continued

ID#	X	Y	V	σ_V	V-R	σ_{V-R}	Radius
26	789.231	736.794	24.535	0.093	0.597	0.127	131.28
27	765.327	591.399	24.274	0.057	0.361	0.097	131.96
28	1019.800	656.992	23.819	0.049	0.644	0.059	135.17
29	1015.400	607.975	24.207	0.046	0.634	0.064	136.11
30	986.392	550.735	24.374	0.055	0.551	0.083	139.81
31	1023.620	670.097	24.347	0.060	0.484	0.086	140.53
32	788.774	543.854	22.378	0.013	0.571	0.028	141.06
33	1030.860	642.657	23.611	0.029	0.674	0.052	145.92
34	1009.710	570.404	23.726	0.034	0.572	0.051	146.35
35	1032.210	650.988	24.256	0.052	0.513	0.074	147.26
36	1006.891	561.630	23.560	0.038	0.487	0.053	148.81
37	737.856	673.300	24.562	0.071	0.448	0.110	149.48
38	1025.050	712.094	23.355	0.027	0.506	0.038	154.44
39	768.297	545.639	23.391	0.030	0.523	0.043	154.58
40	731.862	624.594	23.953	0.045	0.461	0.067	154.77
41	763.646	745.670	24.340	0.068	0.364	0.097	156.40
42	866.209	802.996	24.182	0.064	0.594	0.085	157.12
43	1012.350	747.816	23.393	0.035	0.692	0.050	162.42
44	849.740	813.702	22.862	0.016	0.385	0.029	170.39
45	710.982	640.886	24.314	0.048	0.548	0.082	174.12
46	984.955	502.598	24.186	0.047	0.692	0.061	175.62
47	1058.190	610.010	22.398	0.015	0.663	0.025	177.10
48	1018.550	764.274	24.513	0.048	0.654	0.083	177.73
49	944.464	818.812	23.723	0.038	0.326	0.062	181.81
50	865.038	465.969	25.109	0.022	0.690	0.035	182.13
51	708.124	702.269	24.267	0.062	0.600	0.088	185.31
52	837.989	827.507	24.484	0.101	0.305	0.133	186.53
53	971.376	812.831	24.272	0.044	0.465	0.069	186.98
54	1013.830	509.451	23.829	0.044	0.517	0.056	188.46
55	849.650	460.335	22.978	0.044	0.463	0.067	189.98

Table A.3: HCG 22a photometry—Continued

ID#	X	Y	V	σ_V	V-R	σ_{V-R}	Radius
56	747.976	780.259	24.456	0.075	0.553	0.101	191.14
57	864.687	848.663	23.496	0.023	0.609	0.038	202.68
58	1090.930	618.710	23.249	0.041	0.603	0.068	207.86
59	736.371	487.214	24.357	0.066	0.210	0.127	218.22
60	1062.540	502.050	23.602	0.037	0.544	0.048	229.20
61	776.725	849.930	24.562	0.097	0.093	0.150	230.01
62	655.730	673.944	23.636	0.037	0.603	0.052	230.85
63	834.827	420.180	24.329	0.070	0.890	0.094	232.30
64	1118.600	657.197	23.804	0.032	0.605	0.051	233.82
65	1028.800	457.909	23.257	0.021	0.561	0.033	237.56
66	878.504	884.881	24.295	0.056	0.407	0.085	237.97
67	646.888	652.775	24.533	0.065	0.601	0.101	238.18
68	853.385	408.726	24.220	0.045	0.720	0.057	240.36
69	938.398	887.846	24.338	0.069	0.204	0.113	246.69
70	893.039	400.149	23.820	0.052	0.257	0.066	246.98
71	727.324	455.260	24.373	0.062	0.604	0.073	248.24
72	861.928	894.276	24.036	0.039	0.712	0.055	248.35
73	1067.850	478.448	24.362	0.075	0.461	0.100	248.68
74	1027.700	438.465	23.897	0.057	0.495	0.070	252.68
75	669.169	515.325	23.999	0.055	0.539	0.083	252.83
76	628.934	611.682	24.290	0.052	0.671	0.068	258.49
77	1122.050	521.800	24.495	0.075	0.185	0.110	268.08
78	613.682	630.118	22.995	0.021	0.617	0.031	271.84
79	928.254	372.397	23.721	0.032	0.579	0.042	277.99
80	616.638	721.590	24.466	0.059	0.511	0.087	278.54
81	728.890	888.963	24.315	0.052	0.503	0.074	287.95
82	710.147	875.887	23.204	0.030	0.642	0.045	288.03
83	1069.080	424.792	24.393	0.071	0.312	0.098	288.55
84	661.647	833.556	24.302	0.059	0.525	0.083	291.01
85	1027.270	389.494	22.887	0.046	0.802	0.062	294.19

Table A.4: HCG 22a photometry—Continued

ID#	X	Y	V	σ_V	V-R	σ_{V-R}	Radius
86	1139.700	495.758	23.858	0.037	0.473	0.056	296.22
87	869.448	944.062	24.024	0.051	0.533	0.064	297.47
88	678.099	431.364	24.519	0.083	0.880	0.099	298.84
89	627.361	491.771	22.111	0.010	0.646	0.023	300.79
90	588.557	733.292	23.299	0.019	0.935	0.034	308.75
91	771.524	351.864	24.383	0.064	0.161	0.095	316.20
92	662.858	421.816	23.916	0.044	0.906	0.055	316.31
93	933.859	328.207	23.275	0.022	1.019	0.028	322.52
94	1118.320	870.789	24.463	0.056	0.787	0.077	323.30
95	1107.590	411.256	24.248	0.065	0.386	0.091	324.22
96	650.517	407.871	23.742	0.044	0.575	0.067	334.91
97	936.607	312.903	23.500	0.027	0.725	0.034	338.06
98	538.113	664.504	23.101	0.022	0.595	0.027	347.33
99	1166.840	442.042	23.408	0.024	0.656	0.037	348.48
100	735.687	962.368	24.031	0.064	0.452	0.098	348.93
101	871.643	298.208	23.178	0.024	0.638	0.033	349.05
102	761.830	313.974	24.198	0.058	0.957	0.070	355.07
103	1087.460	354.434	22.641	0.012	1.126	0.017	355.79
104	809.491	287.672	24.102	0.054	0.809	0.067	367.18
105	1127.680	365.203	22.717	0.023	0.648	0.028	371.89
106	1181.720	875.722	23.793	0.033	0.660	0.053	374.64
107	531.065	774.964	22.724	0.019	0.598	0.030	376.36
108	828.431	264.677	24.044	0.045	0.649	0.058	386.48
109	782.635	1025.960	24.541	0.075	0.406	0.116	392.54
110	583.394	390.506	22.732	0.035	0.486	0.050	395.92
111	599.970	922.082	23.893	0.042	0.277	0.072	376.12

Table A.5: HCG 22a photometry—Continued

ID#	X	Y	V	σ_V	V-R	σ_{V-R}	Radius
112	541.864	849.146	24.147	0.068	0.469	0.096	398.25
113	501.962	758.912	24.373	0.055	0.672	0.079	399.05
114	704.125	1007.970	23.307	0.030	0.641	0.040	403.75
115	529.389	454.536	24.401	0.052	0.514	0.089	404.35
116	808.692	1046.370	24.588	0.060	0.256	0.123	406.59
117	1093.340	1003.140	24.109	0.053	0.653	0.071	412.60
118	1245.680	443.196	24.370	0.062	0.664	0.096	414.28
119	1106.940	291.078	22.054	0.015	1.132	0.018	419.45
120	464.563	635.663	24.517	0.072	0.129	0.112	420.590
121	522.787	861.141	22.744	0.017	1.022	0.023	420.78
122	493.912	485.427	23.816	0.039	0.475	0.050	423.15
123	1275.980	814.937	24.327	0.058	0.476	0.091	425.52
124	524.524	410.831	24.524	0.088	0.672	0.115	430.95
125	454.931	583.252	23.436	0.045	0.928	0.068	434.77
126	458.729	758.839	22.266	0.039	0.697	0.062	440.70

Appendix B

Table B.1: Photometry of globular cluster candidates in HCG 90c. All length units are in pixels with X increasing towards the East and Y towards the North (on the sky). The centre of the galaxy is located at X=887 and Y=652.

ID#	X	Y	V	σ_V	V-R	σ_{V-R}	Radius
1	825.304	656.877	24.042	0.088	0.571	0.112	60.51
2	912.768	716.637	22.192	0.050	0.354	0.062	74.97
3	947.235	602.086	23.394	0.084	0.390	0.104	76.75
4	951.138	686.853	23.932	0.078	0.479	0.106	77.22
5	858.053	720.265	23.287	0.043	0.553	0.071	78.06
6	900.303	725.462	23.057	0.041	0.413	0.072	79.94
7	959.514	680.135	23.433	0.058	0.839	0.080	81.55
8	965.661	632.743	23.805	0.082	0.580	0.118	81.91
9	966.772	656.020	23.615	0.065	0.792	0.080	82.27
10	957.269	606.871	24.486	0.102	0.920	0.117	82.66
11	950.923	591.475	24.166	0.096	0.493	0.126	86.19
12	971.951	642.972	22.321	0.070	0.526	0.089	87.04
13	874.289	736.749	22.461	0.040	0.513	0.059	90.38
14	818.795	710.958	24.307	0.092	0.313	0.124	92.05
15	969.971	609.935	24.482	0.112	0.671	0.155	92.70
16	974.792	621.669	23.925	0.079	0.606	0.106	93.30
17	854.453	741.270	24.261	0.106	0.638	0.153	99.10
18	988.019	615.931	23.953	0.050	0.514	0.071	107.60
19	891.467	754.755	23.994	0.114	0.527	0.158	107.95
20	804.469	725.011	23.461	0.054	0.522	0.078	112.12
21	770.504	655.670	24.294	0.084	0.419	0.146	114.82
22	950.797	547.117	22.875	0.075	0.802	0.087	119.61
23	961.444	740.835	22.010	0.024	0.288	0.032	121.03
24	904.758	767.057	24.226	0.101	0.469	0.145	121.67
25	1014.170	610.702	22.220	0.051	0.457	0.073	134.17
26	829.980	774.020	22.814	0.055	0.515	0.077	138.42
27	839.409	777.780	24.537	0.114	0.713	0.141	138.50
28	747.066	669.073	24.323	0.100	0.479	0.146	139.69
29	971.702	757.598	23.707	0.039	0.732	0.062	140.53
30	980.020	753.531	24.259	0.095	0.704	0.131	142.75

Table B.2: HCG 90c photometry—Continued

ID#	X	Y	V	σ_V	V-R	σ_{V-R}	Radius
31	1016.220	705.739	23.150	0.042	0.840	0.063	143.77
32	980.748	759.847	23.177	0.052	0.506	0.071	147.99
33	795.241	768.559	24.560	0.108	0.482	0.144	151.11
34	987.083	531.507	23.343	0.069	0.516	0.088	154.14
35	811.438	785.702	23.666	0.084	0.646	0.102	157.00
36	944.137	499.034	23.494	0.063	0.496	0.090	159.34
37	821.711	796.049	24.123	0.057	0.542	0.095	161.93
38	1045.790	670.109	24.545	0.096	0.967	0.108	162.44
39	767.306	762.270	22.445	0.051	0.520	0.064	164.74
40	968.811	792.641	23.089	0.038	0.532	0.057	168.03
41	1004.910	525.303	22.527	0.051	0.510	0.066	170.85
42	954.506	485.355	22.413	0.044	0.454	0.060	175.96
43	770.415	781.969	24.372	0.084	0.565	0.123	177.05
44	941.947	478.440	24.332	0.087	0.382	0.140	177.92
45	708.374	669.356	24.114	0.093	0.684	0.113	178.04
46	1025.200	534.489	23.414	0.062	0.384	0.087	179.76
47	987.720	801.783	23.474	0.043	0.478	0.060	185.77
48	1074.030	622.940	23.625	0.058	0.667	0.074	190.56
49	1000.810	492.349	24.519	0.077	0.136	0.156	193.21
50	816.458	829.370	24.558	0.110	0.662	0.141	194.82
51	989.522	482.350	22.879	0.057	0.513	0.065	195.02
52	823.961	834.089	24.364	0.074	0.615	0.104	196.79
53	996.216	811.963	24.526	0.080	0.868	0.100	198.95
54	1078.730	601.072	24.344	0.069	0.427	0.108	199.10
55	1085.300	661.857	23.832	0.052	0.612	0.066	200.85
56	776.750	819.823	23.100	0.057	0.560	0.074	203.93
57	1053.490	529.858	23.783	0.046	0.592	0.069	205.21
58	692.496	728.045	23.916	0.066	0.487	0.094	208.87
59	927.725	442.022	24.306	0.113	0.602	0.165	209.38
60	962.016	451.997	24.454	0.135	0.053	0.176	209.66
61	673.401	655.640	24.021	0.056	0.644	0.076	211.78
62	1076.630	556.581	23.009	0.053	0.466	0.070	211.89

Table B.3: HCG 90c photometry—Continued

ID#	X	Y	V	σ_V	V-R	σ_{V-R}	Radius
63	1048.630	786.424	24.444	0.079	0.744	0.100	214.97
64	739.155	808.048	24.550	0.078	0.276	0.127	217.27
65	717.745	787.067	22.732	0.044	0.590	0.059	218.16
66	907.115	429.191	23.582	0.055	0.306	0.070	218.93
67	1030.400	480.546	24.097	0.060	0.360	0.108	221.02
68	692.657	756.715	24.198	0.083	0.583	0.119	221.43
69	662.333	657.789	24.204	0.094	0.710	0.113	222.93
70	934.454	427.957	23.808	0.078	0.692	0.095	224.56
71	1110.630	633.637	23.218	0.047	0.474	0.063	226.02
72	1064.920	787.476	24.350	0.073	0.857	0.102	228.26
73	1110.270	696.255	23.115	0.032	0.319	0.046	230.59
74	699.063	785.103	23.707	0.049	0.717	0.066	231.61
75	665.238	720.396	24.539	0.108	0.355	0.139	231.69
76	1116.720	627.904	24.580	0.105	0.452	0.128	232.50
77	775.371	852.349	24.521	0.068	0.495	0.103	232.78
78	1119.540	638.924	23.861	0.067	0.477	0.083	234.68
79	1113.620	571.337	22.722	0.042	0.413	0.051	240.82
80	937.094	404.577	23.167	0.044	0.553	0.072	247.96
81	963.439	882.306	22.134	0.037	0.660	0.047	248.04
82	769.642	869.461	24.156	0.062	0.268	0.106	250.59
83	993.281	420.879	23.962	0.085	0.718	0.099	250.71
84	810.858	888.660	22.679	0.038	0.444	0.048	252.78
85	641.307	724.860	24.358	0.093	0.518	0.120	255.83
86	629.513	669.665	24.074	0.082	0.712	0.105	256.49
87	952.880	399.153	22.397	0.042	0.158	0.064	256.97
88	690.531	815.431	22.671	0.047	0.445	0.061	257.27
89	673.441	794.657	24.315	0.076	0.692	0.097	257.99
90	655.594	769.311	24.565	0.112	0.719	0.132	259.98
91	945.966	391.322	23.771	0.065	0.601	0.090	262.85
92	627.152	699.638	22.899	0.051	1.098	0.068	263.17
93	715.832	849.668	23.082	0.044	0.605	0.057	263.99
94	1093.220	812.360	23.661	0.047	0.536	0.068	265.89

Table B.4: HCG 90c photometry—Continued

ID#	X	Y	V	σ_V	V-R	σ_{V-R}	Radius
95	1052.180	440.129	23.795	0.054	0.577	0.067	265.98
96	725.148	859.672	24.323	0.067	0.292	0.103	266.05
97	989.289	401.342	22.590	0.053	1.110	0.062	266.88
98	1108.190	491.937	24.215	0.056	0.239	0.093	271.77
99	973.265	388.164	24.086	0.076	1.093	0.092	273.47
100	1145.010	736.661	23.034	0.040	0.628	0.057	275.04
101	798.969	909.341	24.112	0.075	0.532	0.103	276.09
102	1161.250	634.201	23.950	0.044	0.234	0.081	276.55
103	653.885	801.628	24.222	0.090	0.832	0.108	278.07
104	846.118	922.953	22.674	0.031	1.016	0.045	278.68
105	913.206	369.113	24.593	0.087	0.529	0.123	279.31
106	928.282	370.948	24.372	0.100	0.681	0.115	279.42
107	982.487	384.431	22.976	0.029	0.585	0.041	280.08
108	1161.930	692.943	23.531	0.061	0.460	0.075	280.72
109	967.571	378.652	24.123	0.088	0.522	0.122	280.76
110	1059.810	427.103	23.377	0.049	0.460	0.071	280.92
111	715.779	873.142	24.220	0.093	0.570	0.117	282.45
112	963.044	920.066	22.045	0.040	0.909	0.051	284.00
113	1162.530	568.140	24.041	0.069	0.395	0.089	288.52
114	635.719	799.626	24.547	0.102	0.433	0.142	292.29
115	1131.870	484.933	22.902	0.060	0.423	0.068	295.31
116	658.788	837.894	24.436	0.089	0.510	0.115	295.99
117	703.488	882.620	24.370	0.065	1.052	0.077	297.43
118	589.801	689.075	23.276	0.039	0.411	0.064	298.18
119	951.002	941.574	22.920	0.042	1.135	0.050	301.88
120	992.056	364.536	24.006	0.081	0.465	0.103	302.07
121	1105.190	439.974	23.739	0.062	0.791	0.075	302.23
122	1099.860	430.822	23.622	0.064	0.746	0.078	304.79
123	1179.200	739.506	24.338	0.087	0.352	0.120	308.40
124	841.868	954.781	22.804	0.039	0.883	0.058	310.79
125	836.193	959.628	22.002	0.033	0.846	0.048	316.41
126	1060.620	923.381	24.347	0.079	0.424	0.106	327.46

Table B.5: HCG 90c photometry—Continued

ID#	X	Y	V	σ_V	V-R	σ_{V-R}	Radius
127	1130.580	865.655	24.220	0.093	0.000	0.151	328.82
128	577.363	764.440	22.210	0.035	1.194	0.050	329.29
129	1078.610	913.540	24.568	0.095	0.623	0.130	329.44
130	555.220	663.758	24.317	0.090	0.889	0.107	330.20
131	994.211	332.969	24.168	0.085	0.708	0.113	332.48
132	1109.320	892.687	24.352	0.055	1.169	0.078	332.69
133	1055.710	934.306	24.506	0.083	0.347	0.123	334.20
134	955.411	974.367	24.221	0.061	0.507	0.096	334.85
135	948.546	979.059	22.903	0.041	0.572	0.054	338.08
136	893.872	994.875	23.939	0.056	0.967	0.076	347.99
137	1116.550	907.860	24.434	0.089	0.898	0.102	348.80
138	967.012	987.955	23.602	0.045	0.448	0.053	350.68
139	570.348	805.116	24.427	0.097	0.726	0.135	352.14
140	791.622	987.308	23.813	0.056	0.613	0.069	352.89
141	555.996	782.741	24.204	0.073	0.708	0.099	355.91
142	527.521	661.463	24.084	0.053	0.384	0.085	357.77
143	686.338	944.943	22.963	0.028	0.643	0.040	358.10
144	529.437	698.314	22.496	0.041	0.511	0.053	359.25
145	1190.070	457.215	23.040	0.039	0.193	0.051	359.28
146	1231.820	540.234	24.266	0.081	0.364	0.105	362.88
147	1046.030	973.924	24.395	0.075	0.594	0.110	364.43
148	955.680	287.911	24.007	0.068	0.229	0.095	365.98
149	1211.230	479.895	24.234	0.082	0.441	0.105	366.54
150	1142.140	909.653	23.944	0.061	0.520	0.091	367.57
151	1193.570	850.229	24.219	0.082	0.597	0.098	369.48
152	1123.130	932.805	24.189	0.073	1.059	0.087	372.01
153	511.342	675.384	24.353	0.055	0.692	0.087	374.73
154	527.081	764.310	23.073	0.032	0.604	0.047	376.65

Table B.6: HCG 90c photometry—Continued

ID#	X	Y	V	σ_V	V-R	σ_{V-R}	Radius
155	973.312	1013.490	23.893	0.052	1.05 ^o	0.069	376.98
156	705.184	979.454	24.075	0.049	0.45	0.086	377.97
157	562.136	844.958	24.242	0.063	0.602	0.101	378.72
158	1229.330	489.214	23.088	0.038	0.603	0.049	378.76
159	1186.640	416.617	24.336	0.069	0.397	0.105	379.56
160	993.563	279.256	24.241	0.081	0.767	0.091	383.43
161	889.330	260.875	24.525	0.092	0.619	0.127	386.15
162	515.394	760.493	23.563	0.037	0.551	0.054	386.64
163	941.702	263.045	24.300	0.065	0.481	0.092	388.12
164	1019.010	279.705	23.741	0.050	0.407	0.065	390.98
165	1193.230	897.371	22.642	0.032	0.451	0.057	397.10
166	981.104	261.540	24.527	0.083	0.614	0.109	397.26
167	1023.050	272.105	24.269	0.103	0.227	0.136	399.50
168	891.530	1047.240	24.396	0.076	0.716	0.102	400.29
169	498.163	750.376	23.900	0.062	0.412	0.092	400.41
170	1136.940	960.009	23.750	0.057	0.559	0.079	401.81
171	946.457	249.459	22.078	0.032	0.464	0.041	402.26
172	756.119	1029.150	23.098	0.025	0.362	0.055	403.30
173	923.680	1051.940	24.599	0.078	0.471	0.112	406.78
174	1208.030	396.770	24.252	0.086	0.832	0.096	408.61
175	499.900	789.169	24.347	0.064	1.061	0.077	410.50
176	1295.290	612.899	24.132	0.059	0.344	0.095	411.70
177	1089.840	1006.950	23.810	0.064	0.942	0.072	414.15
178	907.171	232.289	24.422	0.098	0.277	0.146	415.30
179	1199.210	373.991	22.506	0.033	0.627	0.045	416.25
180	1235.770	420.582	23.144	0.031	0.298	0.050	417.50
181	1288.780	754.895	23.632	0.037	0.768	0.055	417.95
182	1060.080	265.635	24.374	0.085	0.629	0.104	419.63
183	943.616	1068.120	22.226	0.024	0.454	0.038	425.18
184	1078.690	267.527	23.938	0.076	0.450	0.088	426.05

Table B.7: HCG 90c photometry—Continued

ID#	X	Y	V	σ_V	V-R	σ_{V-R}	Radius
185	745.492	1049.660	24.241	0.117	0.785	0.131	426.14
186	659.447	1008.940	22.396	0.022	0.382	0.035	426.47
187	1000.340	234.792	22.994	0.040	0.512	0.051	428.04
188	976.286	1069.270	23.650	0.045	0.586	0.066	432.02
189	453.467	683.911	24.284	0.076	0.599	0.097	433.11
190	646.540	1010.080	24.474	0.080	0.254	0.128	434.38
191	1156.950	997.645	22.801	0.037	0.469	0.058	443.74
192	784.474	1079.530	24.516	0.074	0.673	0.096	444.06
193	1239.210	370.181	23.443	0.043	1.071	0.054	449.55
194	1064.870	232.951	22.548	0.032	0.402	0.046	451.43
195	1022.540	216.348	24.593	0.102	0.400	0.149	452.08
196	667.722	1046.040	23.520	0.039	0.630	0.062	454.36
197	1271.130	403.857	23.824	0.046	0.534	0.066	456.30
198	860.887	1106.380	24.049	0.077	0.550	0.099	460.01
199	1044.390	214.238	24.237	0.081	0.209	0.108	461.18
200	1317.410	812.536	24.295	0.088	0.090	0.118	463.01
201	1356.080	615.119	23.926	0.051	0.432	0.086	472.16
202	1190.280	1017.880	24.587	0.109	0.544	0.132	480.36
203	1357.600	559.167	24.582	0.104	0.663	0.131	480.69
204	451.276	860.796	24.028	0.055	0.600	0.080	483.55
205	405.370	724.101	22.833	0.035	0.426	0.053	485.79
206	484.762	922.557	24.540	0.078	0.510	0.125	485.92
207	921.228	1135.900	24.567	0.082	0.626	0.109	490.24
208	523.729	980.744	24.193	0.071	0.542	0.099	491.84
209	429.394	833.323	23.780	0.056	0.782	0.084	492.23
210	1280.610	344.545	24.498	0.083	0.447	0.126	497.98
211	1352.670	470.584	23.862	0.055	0.867	0.074	499.84
212	697.555	1113.970	23.957	0.053	0.452	0.073	503.19
213	663.864	1108.110	24.394	0.086	1.011	0.103	511.39
214	700.185	1126.300	24.030	0.056	0.470	0.076	513.70
215	375.840	785.599	23.627	0.053	0.515	0.073	527.69
216	400.763	857.799	23.724	0.058	0.764	0.074	528.13
217	746.055	1156.800	24.116	0.096	0.510	0.114	528.40
218	377.796	796.493	23.610	0.041	0.449	0.062	528.78
219	408.965	890.486	24.021	0.050	0.642	0.079	534.69

Curriculum Vitae

Wayne Alan Barkhouse

University of Toronto
Department of Astronomy
60 St. George st.
Toronto, Ontario
M5S 1A7

Phone: (416) 978-3148
Fax: (416) 971-2026
Email: barkhous@astro.utoronto.ca

Born: Toronto, Ontario, Canada 1964

Education: M.Sc., Astronomy, Saint Mary's University, 1996.
Honour Courses, Dalhousie University, 1993.
B.Sc., Physics, Saint Mary's University, 1992.

Publications:

- 1) Barkhouse, Wayne A., West, Michael J., & Bothun, Greg.,
Globular Cluster Populations of Hickson Compact Groups,
1996, in preparation.
- 2) Barkhouse, Wayne A., West, Michael J., & Bothun, Greg.,
Globular Cluster Populations of Hickson Compact Groups,
Abstract, JRASC, in press.
- 3) Barkhouse, Wayne A., & Mitchell, George F., The Abun-
dance of Atomic Carbon in Outflows, 1996, in prepara-
tion.
- 4) Barkhouse, Wayne A., & Mitchell, George F., The Abun-
dance of Atomic Carbon in Outflows, Abstract, JRASC,
89, 173.

Teaching/Work Experience:

1995/96 Physics Laboratory Demonstrator, Saint Mary's University. Astronomy Course Marker, Saint Mary's University.

1994/95 Physics Laboratory Demonstrator, Saint Mary's University. Astronomy Course Marker, Saint Mary's University. Research Assistant, Saint Mary's University.

1993/94 Physics Laboratory Demonstrator, Saint Mary's University. Telescope Demonstrator, Saint Mary's University.